Experimental Study on the Triaxial Mechanical Behaviors of the Cemented Paste Backfill: Effect of Curing Time, Drainage Conditions and Curing Temperature

Zhanguo Xiu[1†], Shuhong Wang[1✉], Yingchun Ji[2], Feili Wang[1✉†], Fengyu Ren[1]

[1]School of Resources and Civil Engineering, Northeastern University, China.
[2]School of Science, Engineering & Environment, University of Salford, UK.

✉ Corresponding Author: wangshuhong@mail.neu.edu.cn & wangfeili109@126.com
† Co-first author: Feili Wang

Highlights

- Drainage, time and temperature dependent evolution of CPB mechanical properties studied.
- Peak deviator stress and cohesion increase with time and temperature.
- Drained condition can improve the cohesion and reduce the internal friction angle.
- Internal friction angle decreases with time and temperature.
- Vertical stress distribution was affected by different CPB mechanical parameters.

Abstract

The application of CPB (Cemented Paste Backfill) can realize the clean, efficient, and safe mining of underground metal mines. Clear understanding on the triaxial mechanical properties of CPB is important to the CPB design and the stability analysis of the backfilled CPB structure. The triaxial mechanical properties of CPB can be significantly affected by the different curing conditions. In this research, triaxial compression tests of the CPB samples were carried out using the GCTS (*Geotechnical Consulting & Testing System*), and the considered curing conditions include different curing time (1, 3, 7 and 28 days), drainage conditions (drained and undrained) and curing temperatures (20 ℃, 35 ℃ and 45 ℃). The measured mechanical parameters were compared and analyzed against the framework of the Mohr-Coulomb criterion. Then, the vertical stress distribution of the backfilled CPB structure was calculated and discussed using the measured mechanical parameters. The results show that with the increase of the lateral constraint ratio (σ_c/S_{d0}), the elastoplastic stage of the measured deviator stress *versus* axial strain curve of CPB sample is gradually obvious. The peak deviator stress (S_d^p) and the ultimate axial strain (ε^u) show the linear and negative exponential increase with the σ_c/S_{d0} respectively. The number of cracks on the fractured surface of the CPB samples gradually decreased with the increase of σ_c/S_{d0}. The failure types of CPB samples were changed from tensile failure (σ_c/S_{d0} =0%) to the mixed tensile-shear failure ($\sigma_c/S_{d0}\approx$10%) and compression-shear failure ($\sigma_c/S_{d0}\geq$20%). Moreover, with the increase of curing time and curing temperature or under the drained curing condition, the peak deviator stress and cohesion (c_b) of CPB can be significantly increased, but the corresponding internal friction angle (φ_b) is decreased. The shear mechanical parameters of CPB can significantly affect the vertical stress distribution inside the CPB structure. Therefore, when estimating the vertical stress distribution inside the backfilled CPB structure in engineering

practices, it is necessary to focus on the changes of CPB shear parameters (c_b and φ_b) caused by different curing conditions.

Keywords: Tailings; Cemented paste backfill (CPB); Curing time; Drainage condition; Curing temperature; Triaxial test

1. Introduction

As one of the main construction materials for green mining, CPB (a kind of typical cemented tailings backfill, CTB) is widely used in filling mining all over the world (Xu et al., 2020; Qi and Fourie, 2019; Jiang et al., 2019; Bull and Fall, 2020). The filling mining method can not only guarantee the safety of underground miners and mining machines, increase the recovery rate of the valuable ore to bring huge economic benefits, but also minimize the serious environmental problems caused by the random stacking of tailings (Ma et al., 2019; Chen et al., 2018; Deng et al., 2017). The application of CPB has realized the transition from "waste" to "resource" for the tailings. The filling mining method using CPB has been one of the main development trends for the efficient, economical, and pollution-free mining of underground metal mines.

Usually, the CPB slurry is mainly composed of tailings, water, and binder. Among them, the solid content of the uniform slurry is about 70% to 85%, and the binder content is about 3% to 5% (or > 5%, to achieve higher strength) (Nasir and Fall, 2008; Jiang et al., 2018). Sometimes, a small amount of additives are also added to the CPB slurry to obtain better working performance and mechanical properties (i.e. unconfined compressive strength, abbreviated as UCS, shear strength and rheological behavior, etc.) (Pokharel and Fall, 2010; Fang et al., 2020; Xu et al., 2020). Generally, CPB slurry is prepared on the surface and transported to the underground mined-out area by pumping or gravity. The CPB slurry then gradually hardens and consolidates to produce the corresponding strength. The CPB structure, when reached to its design strength, can help resist the deformation of the surrounding rock walls, thereby ensuring the safety of underground mining activities.

The strength indexes of CPB (i.e., UCS, triaxial strength, shear strength, etc.) can provide the basic reference for the optimal design of the filling process. In previous studies, the influence of different factors (for example: solid content, sulfate content and binder content, etc.) on CPB's UCS was studied in detail (Cao and Song, 2017; Li and Fall; 2016; Hou et al., 2020). There were also a number of UCS related studies on CPB including but not limited to: the digital image correlation (DIC) (Xiu et al., 2020), acoustic emission (AE) (Zhou et al., 2020; Zhao et al., 2020), CT (Cao et al., 2021), ultrasonic pulse velocity (UPV) (Yilmaz et al., 2014; Ercikdi et al., 2016; Jiang et al., 2020), numerical simulation (Liu et al., 2017) and other advanced methods were also used to quantitatively analyze the damages of CPB structures. For backfilled CPB structures on site, the mechanical properties of CPB unit located at a given depth were also significantly affected by the lateral constraint stress (σ_3). Tests and analysis (as discussed earlier) focused only on UCS will not truly reflect such case scenarios. Therefore, when lateral constraint stress is present, tests of CPB should be carried out to examine its triaxial mechanical behavior.

For the mechanical behaviors of CPB with lateral constraint stress (or confining pressure σ_c in some literature, $\sigma_3=\sigma_c$), scholars have conducted some relevant experimental studies. Belem et al. (2000) studied the compression behaviors of CPB under the confining pressure (σ_c) of 0~1200 kPa, and the results showed that, with the increase of the binder content, the internal friction

angle (φ_b) of CPB decreased, but the corresponding cohesion (c_b) increased. The dilatancy failure of early CPB during triaxial compression was found by Simms and Grabinsky (2009). In addition, Rankine and Sivakugan (2007) declare that the internal friction angle (φ_b) of CPB in Australia is between 31° and 44°. Behera et al. (2020) evaluated the triaxial compression properties of CPB mixed with fly ash and found that the confining pressure (σ_c) not only affects the mechanical properties, but also determines the failure mode. The PFC^{2D} software was used by Liu et al. (2017) to reproduce the stress-strain curve of CPB and predict the corresponding mechanical properties. Yang et al. (2020) focused on the triaxial mechanical properties of CTB (cemented tailings backfill) with different binder-to-tailings (c/t) ratios at a curing time of 28 days. And several failure criteria were used to effectively calibrate the tested results. Fall et al. (2007) indicate that the peak stress and the stiffness of CPB (curing time lagger than 28 days) are affected by the confining pressure (σc). Xu et al. (2020) indicate that the triaxial compressive behavior of CTB is strongly affected by the cement content, curing age, and confining pressure (σc). And the strength parameter model of CPB under the coupled influence of the particle size distribution and the confining pressure (σc) was constructed by Wu et al. (2018). Also, Wu et al. (2020a; 2020b) conducted the triaxial compression and ultrasonic detection tests to determine the relationship between ultrasonic pulse velocity (UPV) and strength parameters of CPB. Wang et al. (2020) studied the relationship between the strength of layered CPB and the confining pressure (σ_c) under triaxial cyclic loading and unloading conditions. In summary, existing studies indicated that the lateral constraint stress or confining pressure (σ_c) plays an important role on the mechanical behaviors of CPB.

However, the CPB slurry backfilled into the mined-out area is cured in a complex environment (e.g., the difference in curing temperature, drainage conditions, etc.). Varying curing conditions will have influence on the mechanical behavior of CPB. Currently, studies on the influence of different curing time, drainage conditions and curing temperatures on the triaxial mechanical behavior of CPB are lacking. The research proposed in this paper will focus on investigating the influence of curing time (1, 3, 7 and 28 days), drainage and undrained curing conditions, curing temperatures (20℃, 35°C and 45°C) on the triaxial mechanical behaviors of CPB. It is hoped that the findings from this research can improve understanding on the triaxial mechanical behaviors of CPB under various curing conditions and guide the CPB design.

2. Materials and Methods

2.1. Materials

Generally, the slurry of CPB is mainly composed of tailings, binder, and water. In this research, the Ordinary Portland Cement (P.O. 42.5), widely used in CPB applications, was selected as a binder. For tailings, natural tailings (NT) of different mines contain numerous uncertain reactive minerals, and many studies have shown that these complex reactive minerals can significantly affect the basic mechanical properties of the CPB (Ercikdi et al., 2009; Orejarena and Fall, 2010; Fang and Fall, 2019). The artificial tailings (AT) with 99.8% SiO_2 can effectively avoid the unwanted influence of reactive minerals and can adequately represent the NT in examining the CPB mechanical properties. This type of AT has been widely used to investigate

the basic mechanic behavior of CPB (Fall and Nasir, 2010; Fang and Fall, 2018; Xiu et al., 2021). Fig. 1(a) shows the scanning electron microscope (SEM) image of the AT. And the corresponding natural state of AT shown in Fig. 1(d).

To illustrate the rationality of using AT instead of NT, the particle size distribution of AT and the average particle size of 7 mines NT in China were compared and analyzed. As shown in Fig. 1(b), the particle size distribution of AT is close to the average particle sizes of the NT from 7 mines randomly selected in China. And the content of fine particles (<20 μm) is 41.96% (NT) and 39.0% (AT) respectively. Both tailings can be regarded as the fine-grained soil based on the ASTM D2487-17e1(2017). Moreover, the typical shape of NT particle (from Liaoning Province, China) was shown in Fig. 1(c) (Zhang et al., 2020). The same shape of tailings particle between NT and AT can be clearly seen in Figs. 1(a) and (c). Therefore, the difference in mechanical behaviors of CPB caused by shape of tailings particle between NT and AT can be ignored. Hence, the AT is used in this research to avoid the uncertainties which are often caused by the complex reactive minerals in NT.

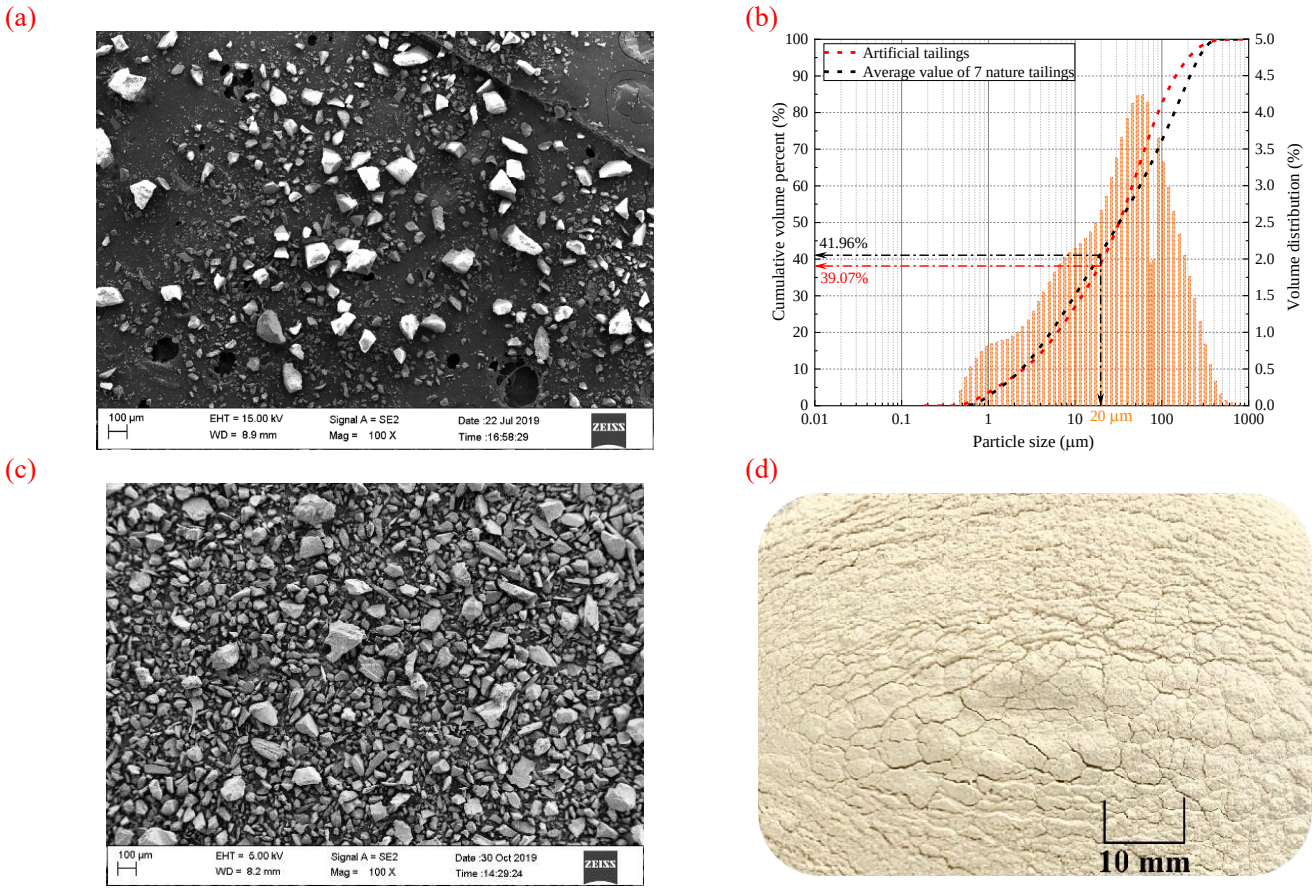

Fig.1 The relevant information about the mentioned tailings: (a) the scanning electron microscope (SEM) image of AT (magnified 100 times); (b) the particle size distribution curves of AT and the average of 7 mines tailings (NT); (c) the SEM image of NT (magnified 100 times) from Liaoning Province, China (Zhang et al., 2020); (d) the natural state of used tailings (AT) in this study.

2.2. Apparatuses used

The GCTS STX-050 triaxial testing system is used to conduct the triaxial compressive tests. The testing system is shown in Fig. 2. The dry compressed air is used to provide the power source for the testing system. And the maximum output air

pressure is 1 MPa. More detailed information about the testing system can be found in Xiu et al. (2020). During the testing process, the sample wrapped by rubber films was placed in the pressure chamber, then the given confining pressure (σ_c) is provided for the sample using hydraulic water. The maximum confining pressure is σ_c=1 MPa. And then, the vertical load acts on the upper surface of the sample to carry out the triaxial compression tests. The servo control system and manual control panel are used to realize the quantitative output of the loading force and confining pressure (σ_c). In the meanwhile, the measured data (e.g., axial strain, deviator stress) were recorded and saved in the computer using the data acquisition system.

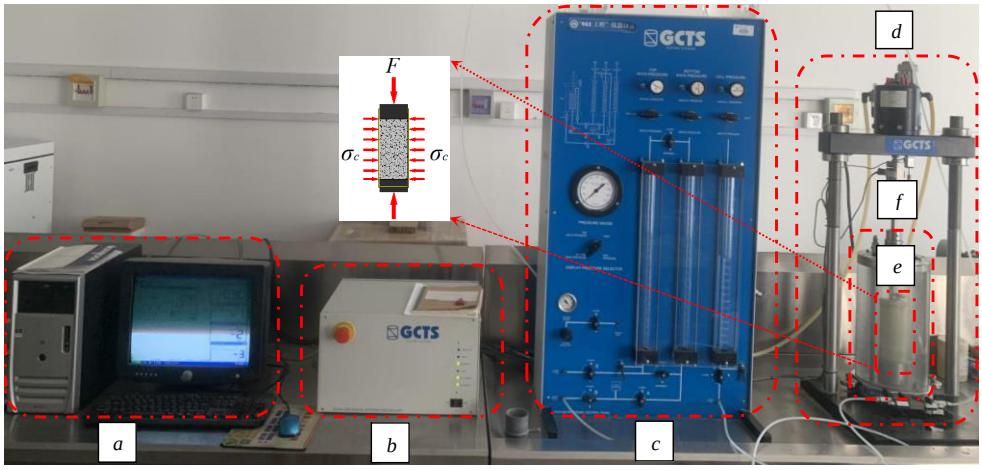

Fig.2 The experimental testing system: a. computer; b. data acquisition system; c. manual control panel; d. loading frame; e. tested sample; f. pressure chamber.

2.3. Sample preparation and testing procedure

The CPB slurry used in this research was a uniform mixture, mixed with dewatered AT, binder and tap water. The three types of materials (AT, binder, water) were stirred in a mortar mixer for 10 minutes to obtain a homogeneous paste, and the paste has 75 wt.% solid content, 7.55 wt.% binder content, and a water-binder ratio (w/b) of 4.75. According to the method suggested by ASTM C143/C143M-15 (2015), for a uniform CPB slurry, the slump of over 18 cm was usually used in practice, and it is the case for the CPB slurry prepared for this research. Then, the uniform slurry was poured into a customized plastic mold and cured in a temperature-controlled curing box at 20℃ ±2℃ for 1, 3, 7 and 28 days (refer to the category A shown in Table 1). After completing the planed curing process, the CPB sample with Φ=50 mm and h=100 mm was prepared.

Three categories were considered to investigate the influence on the triaxial compressive behaviors: (a) category A: four different curing time (1, 3, 7 and 28 days) were considered under undrained condition; (b) category B: drained condition was considered with the curing time for 1 day; and (c) category C: three different curing temperatures (20°C, 35°C and 45°C) were considered during the 1 day curing time. The detailed experimental plan and testing conditions are summarized in Table 1. To investigate the effects of different curing conditions (e.g., curing time, undrained or drained condition, temperature) on the triaxial compressive behaviors, all completed CPB samples were subjected to compressive tests under 4 different confining pressures (σ_c). For the application of CPB, the peak strength is often regarded as an important guidance index. Therefore, the selection of σ_c needs to reasonably consider the difference in peak strength of CPB. In this study, the lateral constraint ratio

(σ_c /UCS) was used to determine the σ_c applied on the CPB samples with different curing conditions. For σ_c /UCS, the UCS (it is equal to S_{d0} in this study) of CPB with different curing conditions was firstly tested, then used as a benchmark. And 0%, 10% 20%, and 30% of the UCS were used to determine the σ_c (approximately, as in Table 1). This means that the choice of σ_c is closely related to the UCS of the CPB samples with different curing conditions. And this selection method of σ_c can make CPB samples with different curing conditions under the same level of lateral constraint stress.

During the compressive tests, the axial loading rate is set at 1 %/min using strain-controlled method (Xiu et al., 2020), and the maximum axial strain is 12%. Also, when the measured residual stress is in a stable stage or the bearing capacity of the tested sample was obviously lost, the loading will be stopped. It is worth to note that, to make sure the measured data are reliable, three identical samples were prepared and tested under the same testing conditions, the averaged measurements from the three identical samples were used for the subsequent analysis.

Table 1. The detailed experimental plans and testing conditions.

Category	Binder content, $B_{wt.\%}$ (%)	w/c ratio	Curing time (days)	Drainage condition	Curing temperature (°C)	Lateral constraint ratio (σ_c/S_{d0}, %)
A	7.55	4.75	1	Undrained	20	0, 10.05, 20.10, 30.14
A	7.55	4.75	3	Undrained	20	0, 9.63, 19.07, 28.71
A	7.55	4.75	7	Undrained	20	0, 9.97, 19.93, 29.90
A	7.55	4.75	28	Undrained	20	0, 10.03, 20.05, 30.08
B	7.55	4.75	1	Drained	20	0,9.99, 19.99, 29.98
C	7.55	4.75	1	Undrained	35	0, 9.98, 19.96, 29.94
C	7.55	4.75	1	Undrained	45	0, 10.03, 20.07, 29.94

Note: $B_{wt\%} = 100\%*M_{binder}/M_{dry\text{-}tailings}$. Where, M_{binder} is the mass of binder; $M_{dry\text{-}tailings}$ is the mass of dry tailings. σ_c is the confining pressure; S_{d0} is the peak deviator stress under σ_c=0 kPa (S_{d0} is equal to the UCS in the value).

3. Experimental Results

3.1. Influence of curing time on the triaxial compressive behaviors

Once the CPB slurry is backfilled into the underground mined-out area, the strength of backfilled CPB is gradually developed by the action of consolidation and hardening. Due to CPB slurry contains numerous cement particles (P.O. 42.5), the degree of cement hydration is closely related to curing time. The hydration products (e.g., C-H; C-H-S gel, etc.) inside CPB gradually increase with the curing time (Xiu et al., 2021). The strength of the CPB is mainly provided by the cohesive force generated by the bonding between the hydration products and the tailings particles. Therefore, the triaxial compressive behaviors of CPB is also closely related to the curing time. It is worth noting that understanding the triaxial mechanical behaviors of the CPB at early stages after backfilled is important to determine when it is appropriate to open barricades, which helps reducing mining cycle time and increasing mining efficiency and production. Therefore, the curing time from 1 to 28 days was selected in this study. The effect of curing time on the triaxial compressive behaviors will be closely assessed in this section.

The deviator stress *versus* axial strain curves of CPB samples under different curing time (1, 3, 7 and 28 days) with different lateral constraint ratios (σ_c/S_{d0}≈0%, 10%, 20% and 30%) are shown in Fig. 3. It can be seen from Fig. 3 that each curve has a clear peak point (peak deviator stress). And with the increase of the axial strain (ε_a), the deviator stress (S_d) was gradually

increased to the peak value and then decreased. The characteristic of strain softening can be clearly seen from the measured deviator stress *versus* axial strain curves of CPB samples. Moreover, with the increase of σ_c/S_{d0} (from 0%, 10%, 20% to 30%), regardless of the curing time, the peak deviator stresses (S_{d0}, S_{d1}, S_{d2} and S_{d3}) of the CPB samples are increased, and the corresponding ultimate axial strain values (ε_0^u, ε_1^u, ε_2^u and ε_3^u) which resulted the peak deviator stresses are also increased. This observation is clear evident for all the curing times (1, 3, 7 & 28 days) as illustrated in Fig. 3.

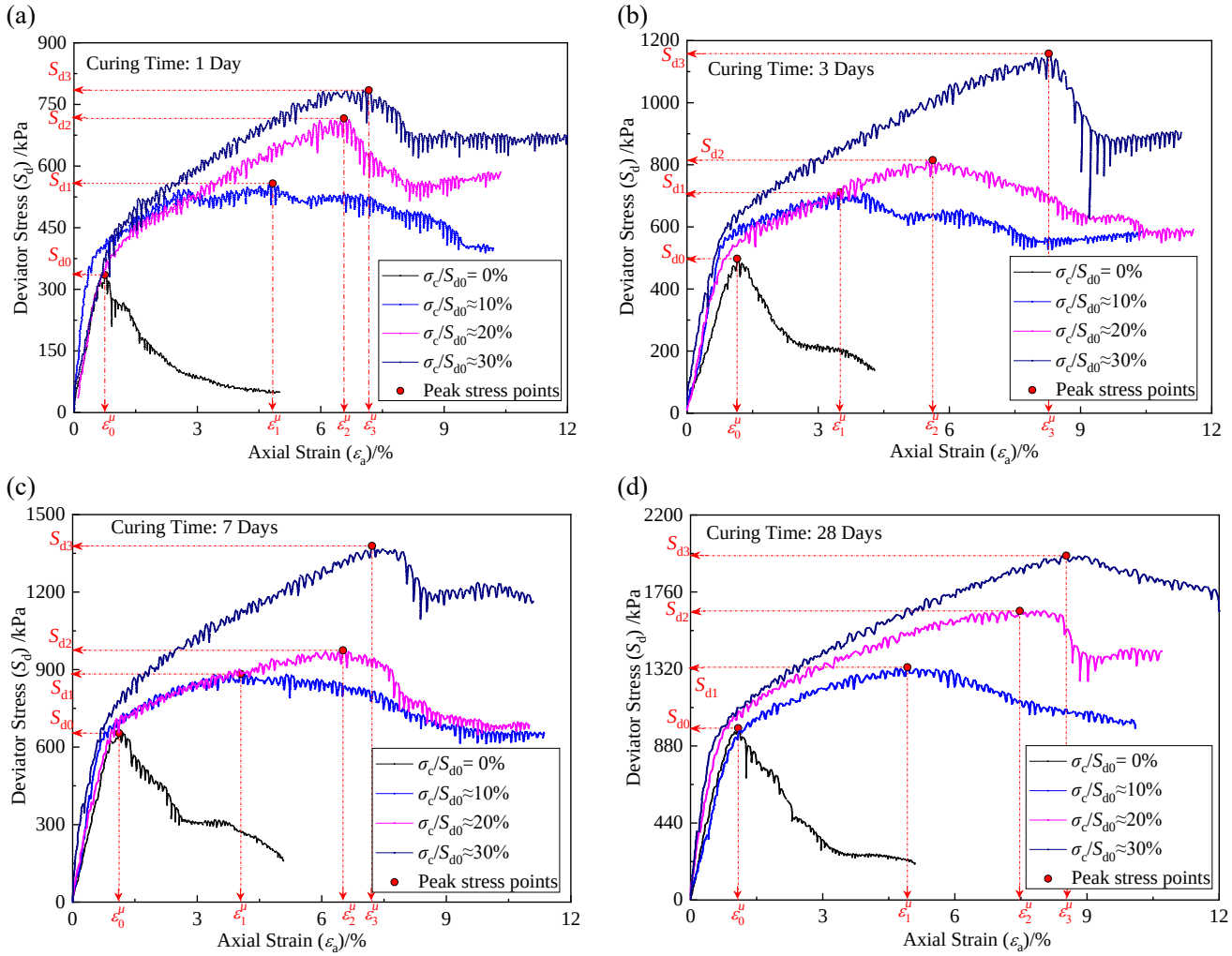

Fig.3 The deviator stress of CPB samples *versus* axial strain curves under different curing time with different lateral constraint ratios (σ_c/S_{d0}≈0%, 10%, 20% and 30%): curing time for (a) 1 day; (b) 3 days; (c) 7 days; and (d) 28 days.

To closely examine the influence of σ_c/S_{d0} on the deviator stress *versus* axial strain curve, the typical tested curves with the curing time of 28 days were selected (Fig. 4). When the σ_c/S_{d0}=0%, as shown in Fig. 4a, the deviator stress *versus* axial strain curve of the tested CPB sample can be clearly distinguished by two stages: the deviator stress rapid growth stage (the linear elastic stage, *O*~*A* section) and the rapid decline stage of deviator stress (the failure stage, *B*~*C* section). However, the elastoplastic stage (*A*~*B* section) is not obvious under the test condition of σ_c/S_{d0}=0%. If the lateral constraint stress was applied on the CPB sample during the compressive tests (i.e., $\sigma_c/S_{d0} \neq 0$), due to the dilatancy of the CPB sample, its plastic deformation will be increased significantly. For example, when the σ_c/S_{d0}≈10%, the deviator stress *versus* axial strain curve can be clearly divided into three stages shown in Fig. 4b: the rapid growth stage of the deviator stress (the linear elastic stage,

O'~*A'* section), the slow growth stage of the deviator stress (the elastoplastic stage, *A'*~*B'* section) and the decline stage of the deviator stress (the failure stage, *B'*~*C'* section). Furthermore, with the increases of parameter σ_c/S_{d0}, the span of axial strain in the elastoplastic stage gradually increases (shown in Figs. 3a~3d). The increase of the peak deviator stress and ultimate axial strain of the CPB samples with the σ_c/S_{d0} can be called the "dilatancy strengthening effect".

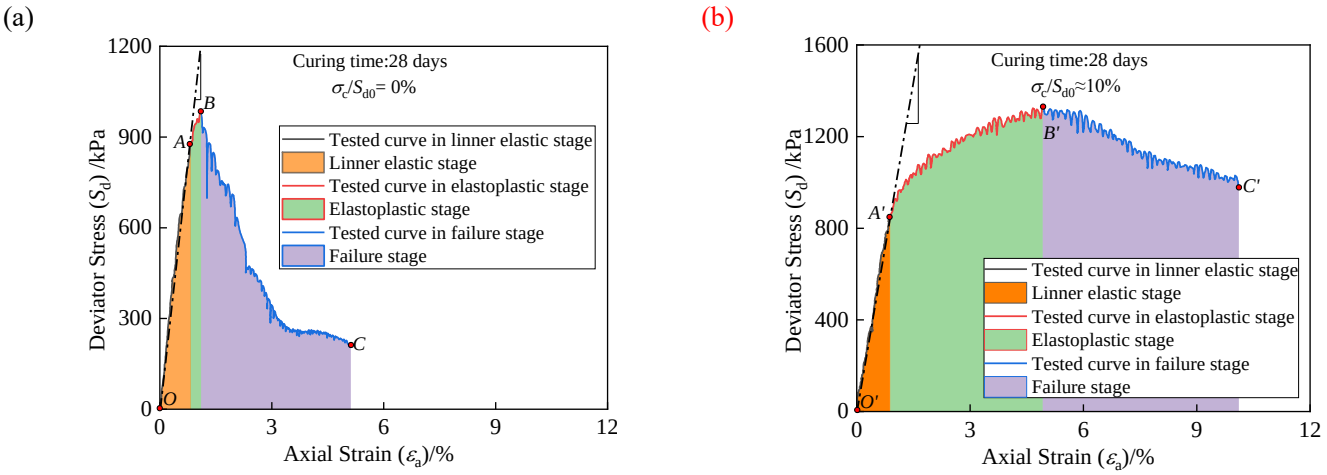

Fig.4 The typical deviator stress *versus* axial strain curves with curing time of 28 days: (a) σ_c/S_{d0}=0%; (b) σ_c/S_{d0}≈10%.

Fig. 5(a) shows the relationship between different σ_c/S_{d0} values and peak deviator stress. The peak deviator stress (the averaged measurement from three identical samples) gradually increases with the increase of σ_c/S_{d0} under the same curing time. A strong linear relationship between σ_c/S_{d0} and peak deviator stress is evident from the measured results, as shown by the linear fitting of measured data in Fig. 5a ($y=b+ax$, where y is the peak deviator stress; x is the lateral constraint ratio σ_c/S_{d0}; a and b are the fitting parameters, respectively). The relationship between peak deviator stress (S_d^p) and curing time (D) is shown in Fig. 5(b), a clear power function relationship can be established between the peak deviator stress and the curing time under the same σ_c/S_{d0} value.

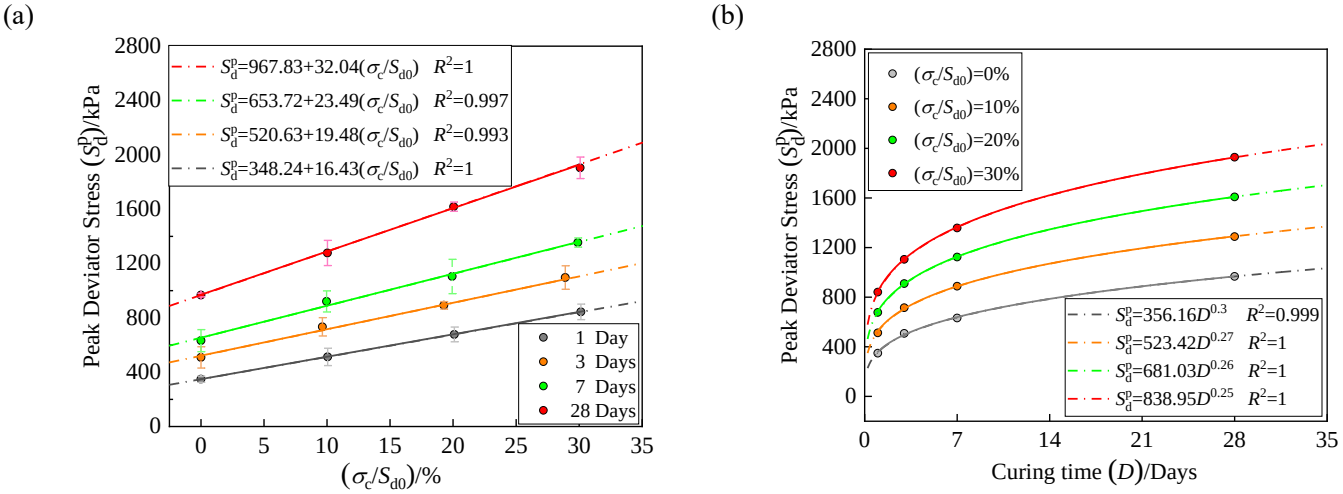

Fig.5 The effects of σ_c/S_{d0} (a) and curing time (b) on the peak deviator stress.

It should be noted that the power function was used to establish the fitting curves in Fig.5b. The figure indicates that the yield stress of the freshly mixed CPB slurry tends to be 0. Several studies have shown that the yield strength of the freshly mixed CPB slurry is less than 1 kPa (e.g., Simon and Grabinsky, 2012; Jiang et al., 2016). This yield stress of the freshly mixed CPB

slurry is much smaller than the UCS (from 348.34 kPa to 967.57 kPa) of CPB samples in this study. Therefore, it is reasonable to assume that the yield stress of freshly mixed CPB slurry is 0 in this study. With this assumption, the power function is the most consistent fitting method against the tested results. The power function fitting ($y=cx^b$) describes the relationships between the curing time and the peak deviator stresses under different σ_c/S_{d0}, where c and d are the corresponding fitting parameters in the fitting formula; y is the peak deviator stress; x is the curing time.

Fig. 6 shows the relationship between σ_c/S_{d0} and the ultimate axial strain (the averaged measurement from three identical samples) by fitting their measured data. The figure clearly indicates that the ultimate axial strain of the CPB sample exhibits a negative exponential growth with σ_c/S_{d0}. The data fitting is based on an exponential relationship ($y=e$*exp(-x/f)+g, where, e, f and g are the corresponding fitting parameters, respectively; x is the σ_c/S_{d0}; y is the ultimate axial strain.). It clearly evidents from Fig. 6 that the-ultimate axial strain is not sensitive with the curing time, the variation in ε_a^u is rather small with four ratios of σ_c/S_{d0} tested.

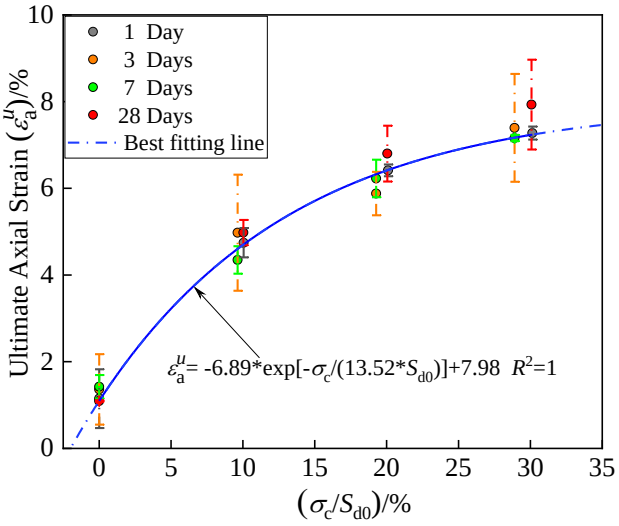

Fig.6 The exponential relationship between σ_c/S_{d0} and ultimate strain (ε_a^u).

Triaxial compressive tests can also assess other important parameters of CPB, such as the internal friction angle (φ_b) and cohesion (c_b). These two parameters can be directly obtained using the Mohr-Coulomb strength envelope. Fig. 7 shows a schematic diagram of the distance from the Mohr stress circle to a random straight line. The center coordinate of Mohr stress circle shown in Fig.7 is ((σ_c+σ_1)/2, 0), and its radius is (σ_1-σ_c)/2. Then, the distance ($\delta = |PM|$) from the Mohr stress to the straight line ($\tau = c_b + \sigma \tan\varphi_b$) can be calculated by formula (1):

$$\begin{aligned}\delta &= |PM| \\ &= \left(\frac{c_b}{\tan\varphi_b} + \frac{\sigma_1+\sigma_c}{2}\right)\sin\varphi_b - \frac{\sigma_1-\sigma_c}{2} \\ &= \left(\frac{\sigma_1+\sigma_c}{2}\sin\varphi_b + c_b\cos\varphi_b\right) - \frac{\sigma_1-\sigma_c}{2}\end{aligned} \quad (1)$$

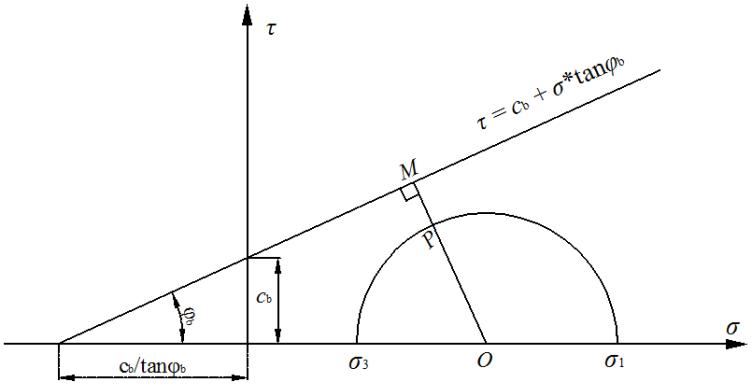

Fig.7 Schematic diagram of the distance from any straight line to the Mohr stress circle (here σ_3 is the third principal stress, the same as the lateral constraint stress, σ_3 equals the confining pressure σ_c, σ_1 is the first principal stress.).

Usually, the straight line ($\tau = c_b + \sigma \tan \varphi_b$) is obtained from a common envelope for a group of Mohr stress circles. To obtain the suitable straight line ($\tau = c_b + \sigma \tan \varphi_b$), the total distance (Δ) from a random straight line to the group of Mohr stress circles should be calculated firstly using formula (2):

$$\Delta = \sum_{i=1}^{n} \delta_i \tag{2}$$

Where, n ($n \geqslant 3$) is the number of tested Mohr stress circle.

When the total distance (Δ) takes the minimum value, the linear formula to be sought is the common envelope for the group of the Mohr stress circles. In formula (1), assuming that $\frac{\sigma_1 + \sigma_c}{2} = x$, $\frac{\sigma_1 - \sigma_c}{2} = y$, $\sin \varphi_b = B$, $c_b \cdot \cos \varphi_b = A$, then, the total distance from a random straight line to the group of Mohr stress circles can be calculated using followed formula (3):

$$\Delta = \sum_{i=1}^{n} \delta_i = \sum_{i=1}^{n} \left[(Bx_i + A) - y_i \right] \tag{3}$$

When $\delta_i \to 0$, $\Delta = \sum_{i=1}^{n} \delta_i$ takes the minimum value. Therefore, a linear regression analysis of formula (3) is adequate to determine the values of A and B, when $\delta_i \to 0$. Then, the internal friction angle (φ_b) and cohesion (c_b) can be obtained by the following formula (4):

$$\varphi_b = \sin^{-1} B; \quad c_b = \frac{A}{\cos \varphi_b} \tag{4}$$

With the formulas described above (formulas 1~4), the internal friction angle (φ_b) and cohesion (c_b) of CPB under different curing time (1, 3, 7 and 28 days) can be calculated using the measured data (S_{d0}, S_d, σ_c, σ_1 as shown in Table 2 and Fig. 8). It can be seen from the calculation results that the cohesion (c_b) is gradually increased with the curing time. However, the internal friction angle (φ_b) is gradually reduced with the curing time.

Fig. 8 shows the positional relationship between the Mohr stress circles and the Mohr-Coulomb strength envelope of the CPB samples under different confining pressures and curing times. The Mohr-Coulomb strength envelope has a good tangent

relationship with the Mohr stress circles. The linear expression of the Mohr-Coulomb strength envelope is the Mohr-Coulomb strength criterion under the corresponding testing conditions (shown in Figs. 8(a-d)). And the intercept of the linear expression is the cohesion (c_b), and the slope is the internal friction angle (φ_b).

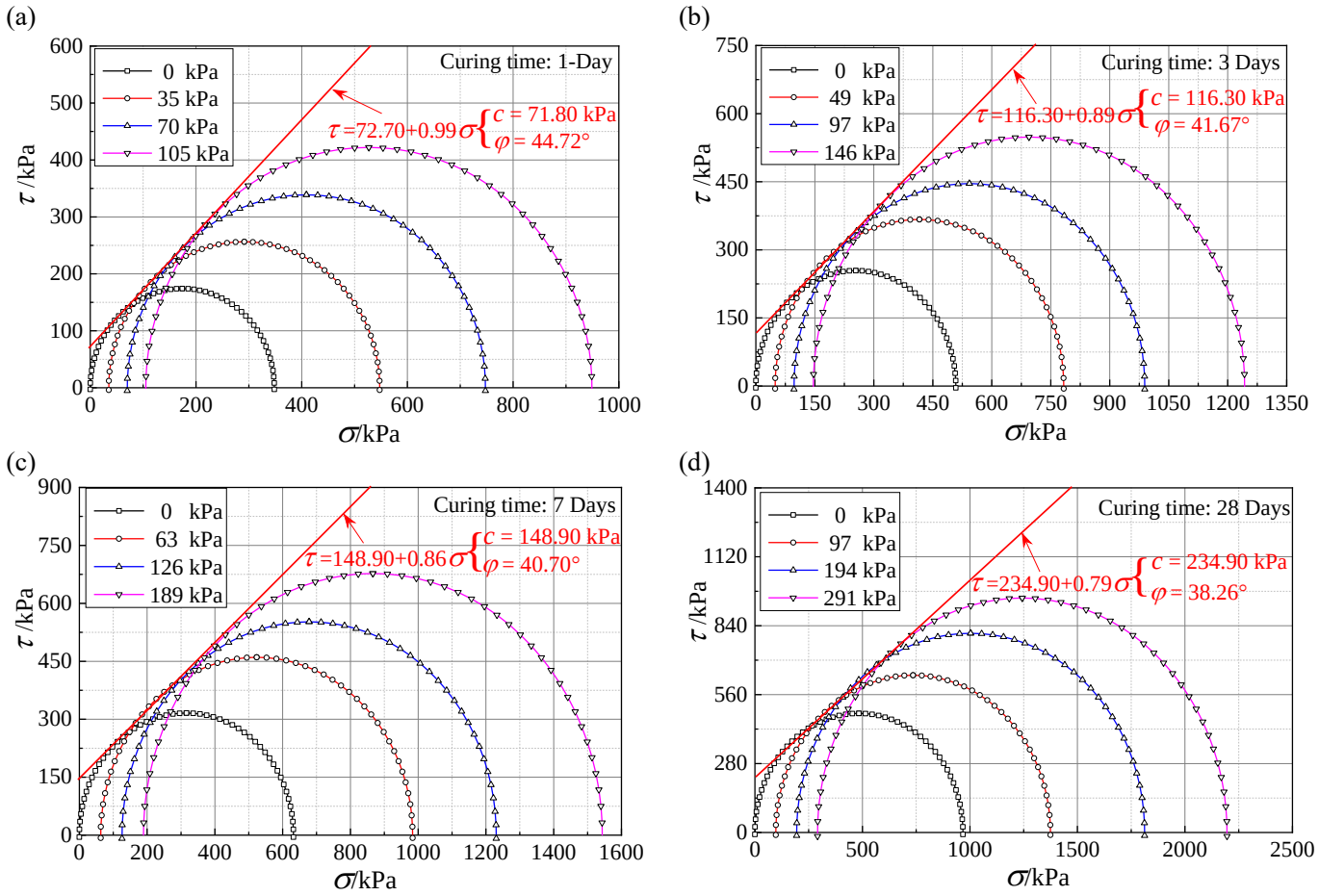

Fig.8 The positional relationship between the Mohr stress circles and the Mohr-Coulomb strength envelope of the CPB samples under different confining pressures and curing times: (a) curing time for 1 day; (b) curing time for 3 days; (c) curing time for 7 days; (d) curing time for 28 days.

Table 2 The calculated internal friction angle (φ_b) and cohesion (c_b) under different curing times using measured data.

Curing time (days)	Stress state (kPa)					Internal friction angle (φ_b/°)	Cohesion (c_b/kPa)
	S_{d0}	S_d	σ_c	$(\sigma_1+\sigma_c)/2$	$(\sigma_1-\sigma_c)/2$	$\sin^{-1}B$	$A/(\cos\varphi_b)$
1	348.34	348.34	0	174.17	174.17	44.72	71.80
		512.67	35	293.34	256.34		
		677.71	70	408.86	338.86		
		844.14	105	527.07	422.07		
3	508.58	508.58	0	254.29	254.29	41.67	116.30
		734.02	49	416.01	367.01		
		892.04	97	543.02	446.02		
		1097.05	146	694.53	548.53		
7	632.06	632.06	0	316.03	316.03	40.70	148.90
		920.82	63	523.41	460.41		
		1104.52	126	678.26	552.26		
		1354.69	189	866.35	677.35		
28	967.57	967.57	0	483.785	483.79	38.26	234.90
		1277.55	97	735.775	638.78		
		1618.63	194	1003.315	809.32		
		1904.77	291	1243.385	952.39		

To quantify the relationship between the shear parameters (internal friction angle, φ_b and cohesion, c_b) of the CPB samples

and the curing time, data fitting was performed on the calculated shear parameters and the corresponding curing time. As shown in Fig. 9, exponential relationships between the shear parameters (φ_b and c_b) of the CPB samples and the curing time were established. The early curing time (from 1 to 7 days) has a greater effect on the shear parameters of CPB samples.

To understand the strength of CPB and controlling the cost of backfill at early design stages, it is very important to have the ability to predict the peak deviator stress of CPB under different lateral constraints stress (confining pressure, σ_c) and curing time (D). Fig. 5(a) shows a linear relationship ($y=b+ax$) between the peak deviator stress ($y=S_d^p$) and the lateral constraint ratio ($x=\sigma_c/S_{d0}$) and this relationship can be used to predict the peak deviator stress providing the fitting parameters a, b and S_{d0} are known at a specific curing time (D) and confining pressures (σ_c). With the measured data at 1, 3, 7 & 28 days curing time in this research, an exponential relationship between fitting parameters (a and b) and curing time can be established. Fig. 10 shows the correlation between curing time and the fitting parameters, i.e., once curing time (D) is known, the parameters a, b can be obtained using the relevant exponential function.

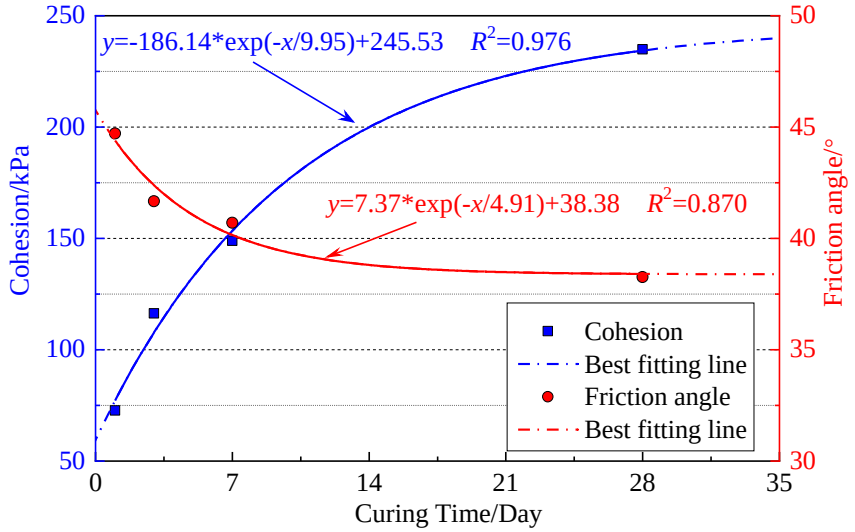

Fig.9 The relationship between the calculated shear parameters (internal friction angle, φ_b and cohesion, c_b) and the different curing time.

The parameter S_{d0} is the UCS of the CPB samples. The parameter S_{d0} and the curing time (D) conform to the power function relationship (the corresponding fitting formula is shown in Fig. 5b, gray line). The best fitting formulas (shown in Figs. 10 and 5b) of parameters (a, b and S_{d0}) are brought into formula (5), then, the peak deviator stress regression formula (5) of CPB under different lateral constraints stress (confining pressure, σ_c) and curing time (D) can be obtained:

$$\begin{aligned} S_d^p &= a+b\cdot(\sigma_c/S_{d0})\cdot 100\% \\ &= \frac{\sigma_c}{\xi_{1d}D^{\xi_{2d}}}(\xi_{3d}e^{\frac{-D}{\xi_{4d}}}+\xi_{5d})\cdot 100\%-\xi_{6d}e^{\frac{-D}{\xi_{7d}}}+\xi_{8d} \end{aligned} \tag{5}$$

Where, ξ_{1d}~ξ_{8d} are the corresponding fitting parameters.

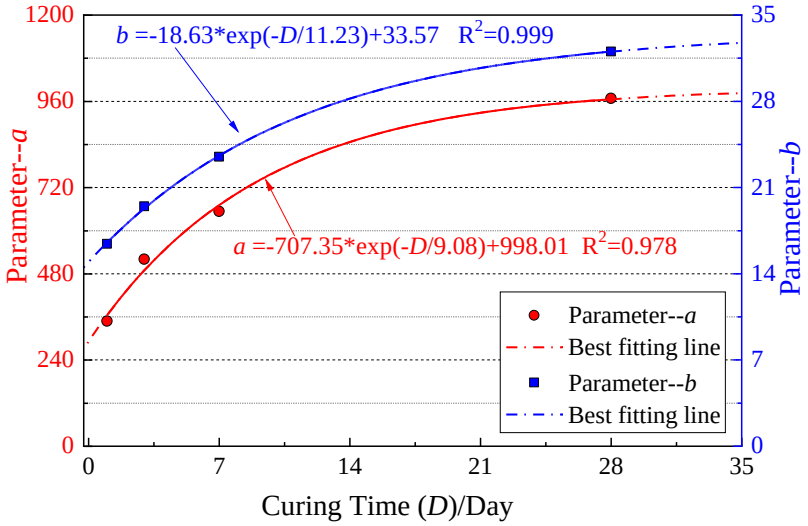

Fig.10 The relationship between fitting parameters (a and b) and curing time (D).

Formula (5) can realize the prediction function of peak deviator stress under different curing time (D) and different depth (confining pressure, σ_c). Fig. 11(a) shows the comparison between the calculated values using formula (5) and the measured values of the peak deviator stress for the CPB samples. It can be seen from Fig. 11(a) that the measured results are closely distributed around the straight line (measured values/calculated values=1:1). This shows that the regression model established in this paper (formula 5) can well predict the peak deviator stress of CPB samples. Furthermore, under a given curing time, the shear parameters (internal friction angle, φ_b and cohesion, c_b) can also be estimated by formula (5) under different confining pressure (σ_c). Fig. 11(b) shows that the calculated and measured values of shear parameters (internal friction angle, φ_b and cohesion, c_b) for the CPB samples agree with each other consistently, which indicates the ability of formula (5) in predicting the relevant shear parameters. Such predictions can provide robust guidance for the strength design and cost control of the CPB structure in engineering practice.

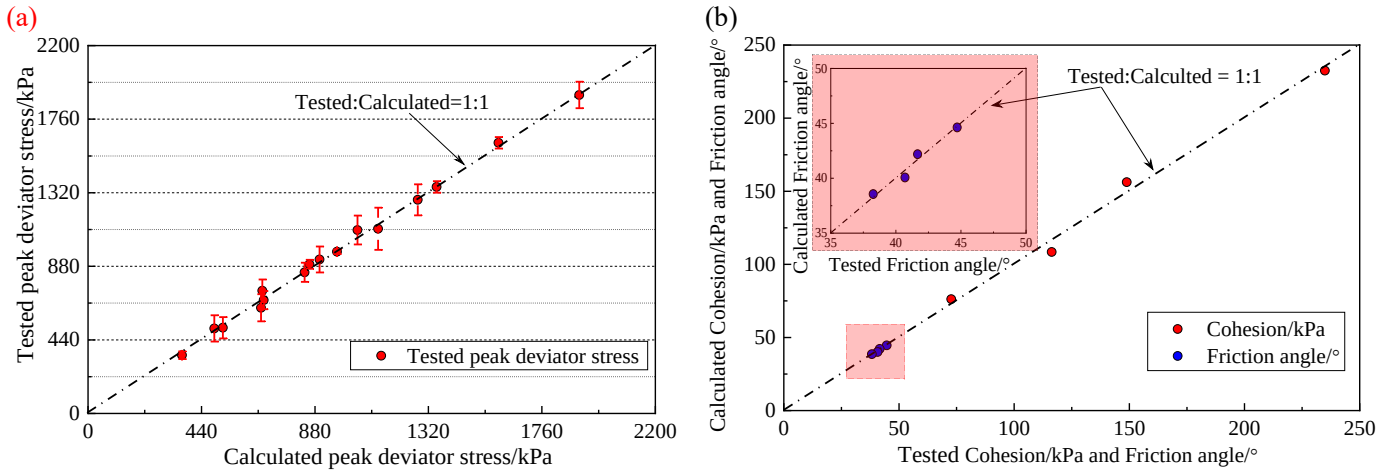

Fig.11 Comparative analysis of calculated and measured results: (a) the peak deviator stress; (b) the shear parameters (internal friction angle, φ_b and cohesion, c_b).

3.2. Influence of drainage conditions on the triaxial compressive behaviors

The barricade at the bottom of the underground mine-out area can be considered as drain or undrained conditions due to the

different permeability of the surrounding rock walls in many on-site conditions. Therefore, the CPB slurry filled into the underground mine-out area will inevitably experience different drainage conditions. The difference in drainage conditions in turn will have an important influence on the triaxial compressive behaviors of CPB.

Fig. 12 shows the typical deviator stress *versus* axial strain curves of CPB samples with drained conditions and curing time for 1 day under different lateral constraint ratios ($\sigma_c/S_{d0}\approx$0, 10, 20 and 30%). Compared with the corresponding deviator stress *versus* axial strain curves under undrained conditions (shown in Fig. 3a), it is fair to say the changing trend of the tested curves for both the undrained and drained conditions are similar. Between the drained and undrained conditions, there are clear differences in the peak deviator stress (S_{d0}, S_{d1}, S_{d2} and S_{d3}) and the ultimate axial strain (ε_0^u, ε_1^u, ε_2^u and ε_3^u) required to reach the corresponding peak deviator stress. The following discussions will focus on the influence of the difference of drainage conditions on the peak deviator stress, ultimate axial strain and shear parameters (internal friction angle, φ_b and cohesion, c_b) of CPB samples prepared for this study.

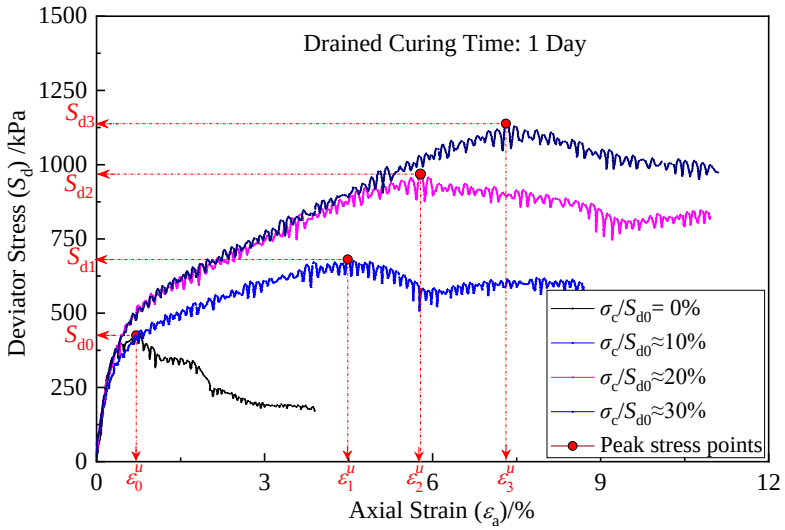

Fig.12 The typical deviator stress *versus* axial strain curves under different lateral constraint ratios (with drained condition and curing time for 1 day).

Fig. 13 shows the changing relationship of the measured peak deviator stress (S_d^p) and the ultimate axial strain (ε_a^u) of CPB under drained and undrained curing conditions with the increase of the lateral constraint ratios ($\sigma_c/S_{d0}\approx$0, 10, 20 and 30%). As shown in Fig. 13a, for both drained and undrained condition curing for 1 day, the peak deviator stresses (S_d^p) of CPB samples show clear linear relationship against lateral constraint ratio σ_c/S_{d0}. While under the same σ_c/S_{d0}, the peak deviator stress of the CPB cured under drained condition is consistently higher than that under the undrained condition. However, for the ultimate axial strain (ε_a^u) (as shown in Fig. 13b) required to reach the peak deviator stress (S_d^p), it is marginally affected by the drained or undrained curing conditions. As the σ_c/S_{d0} increased, the ultimate axial strain (ε_a^u) is increased exponentially. This observation is similar to the corresponding results under different curing time (refer to the Figs. 5a and 6), so the influence

from difference drainage conditions on the ultimate axial strains of CPB is negligible.

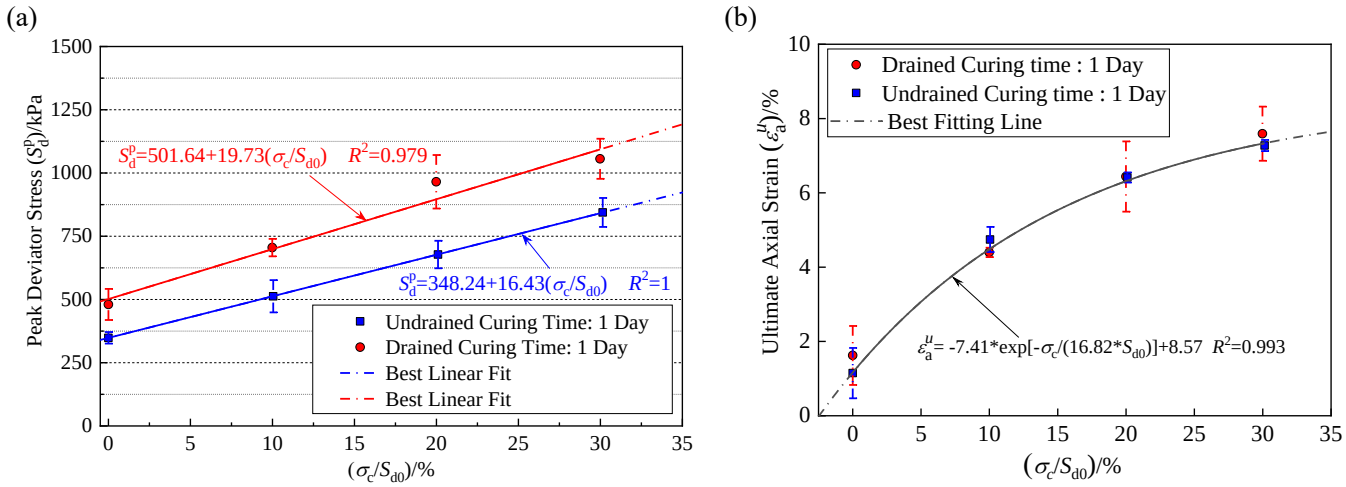

Fig.13 When the lateral constraint ratio is increased ($\sigma_c/S_{d0} \approx 0$, 10, 20 and 30%) under drained and undrained curing conditions for the CPB samples tested, the corresponding changes of: (a) the peak deviator stress (S_d^p) and (b) the ultimate axial strain (ε_a^u).

To investigate the underlying reasons of the difference in measured deviator stress of CPB caused by the different drainage conditions for 1 day curing time, the internal pore water pressure (PWP) of the CPB slurry was monitored. Fig. 14 is a schematic diagram of pore water pressure monitoring equipment. The CPB slurry is placed in a 100*50 mm cylindrical mold (the drainage hole was provided at the bottom of cylindrical mold to facilitate the drainage and undrained conditions during the curing process), and a geotechnical filter paper is placed at the bottom of the CPB slurry to prevent CPB slurry drained through the drainage hole. The CPB slurry was placed in a temperature-controlled curing box (the temperature is set to 20℃ ±2℃). The PWP sensor and the middle position of the CPB sample were connected by a thin hose. The thin hose is filled with water to ensure that the PWP can be accurately transmitted to the PWP sensor. The data acquisition system can monitor the PWP inside the CPB sample in real-time.

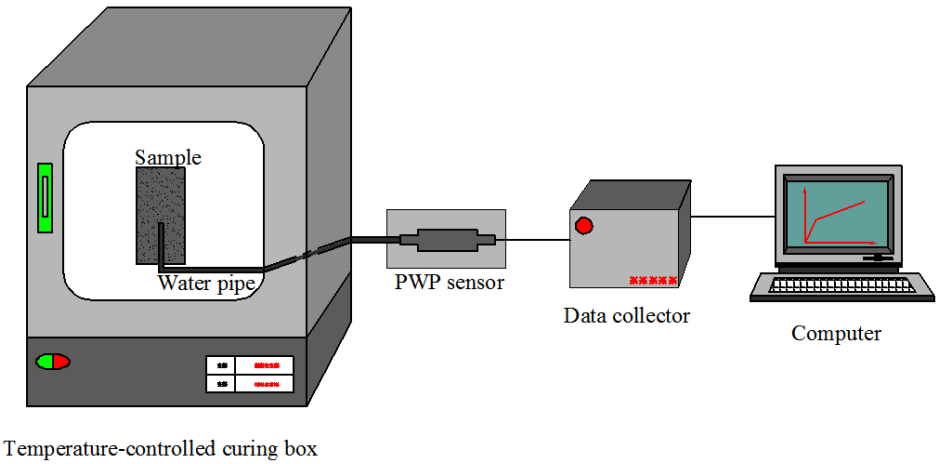

Fig.14 The schematic diagram of pore water pressure (PWP) monitoring equipment.

Fig. 15 shows the variation of the PWP inside the CPB samples during the 1-day curing process under drained and undrained

conditions. For both conditions, the measured PWP inside the CPB samples would increase roughly during the first 4 hours and then gradually decrease during the rest of the day, moving into negative PWP (PWP＜0). The negative PWP curing condition (the effective stress will be increased inside the sample, $\sigma' = \sigma - \text{PWP}$. Where, σ' is the effective stress; and σ is the total stress.) will have a positive effect on the strength growth of the CPB sample (Fang and Fall, 2020; Ghirian and Fall; 2013).

In undrained condition, the changing trend of PWP can be roughly divided into two stages, stage 1: the slow increase of PWP; and stage 2: the slow decrease of PWP. However, in drained condition, the variation of PWP can be divided into three stages: stage 1: the rapid increase of PWP; stage 2: the rapid decrease of PWP; and stage 3: the slow decrease of PWP to the stable stage. With the drained curing condition, the PWP in the stage 1 increases much more than that of the undrained condition. In stage 1, the CPB slurry is in a fluid state. In this state, the solid particles suspended in the slurry will settle under the action of their own weight. As the solid particles in the upper part of the fluid slurry move to the lower part of the slurry, the PWP inside the sample will be rapidly increased. When the sample is cured by drained condition, the water is continuously discharged from the CPB slurry, which drives the settlement of solid particles and causes a larger increase in PWP (stage 1) than that with undrained curing condition. It is also worth to note that the duration of stage 1 under the drained curing condition is slightly longer than that under the undrained curing condition (h_d＞h_u, about at the fourth hour). This phenomenon is caused by the continuous disturbance of the solid particles during the discharge of the water in the CPB slurry. At about the fourth hour, the CPB slurry is in a critical stage between the skeleton formation and liquid state (Hou et al., 2018). At the critical moment, since the settlement of tailing particles has stopped, the water inside the CPB slurry has been consumed to participate in the hydration reaction, the PWP was dissipated by this hydration reaction. Therefore, the peak points of PWP at about fourth hour in Fig 15 was found.

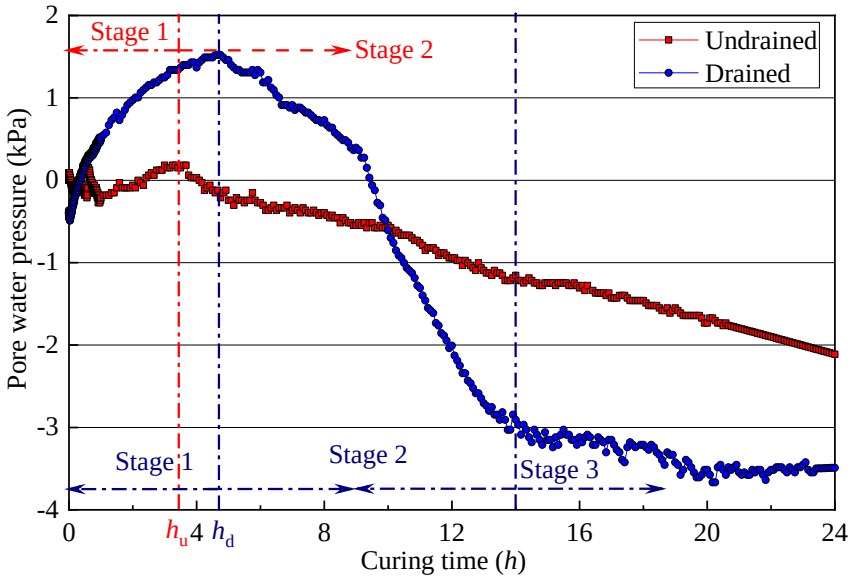

Fig.15 The changing trend of the PWP inside the CPB samples during the 1-day curing process under drained and undrained conditions.

When the settlement of solid particles is gradually completed, the strength will be formed inside the CPB sample. The autogenous shrinkage is caused by the hydration reaction of the cement particles in the CPB slurry. This phenomenon will cause a decrease in PWP, gradually leading to a negative PWP inside the CPB. The negative PWP inside the CPB causes the increase of the effective stress. The solid particles of CPB are crowded with each other by the action of the effective stress, which has a positive effect on the increase of strength. Because the CPB slurry is in a closed mold under undrained curing condition, the PWP inside the CPB shows a slow decrease process (stage 2 for undrained curing condition shown in Fig. 15). However, for drained curing condition, there is an obvious stage 3 by examining the PWP curve. Due to the action of negative PWP inside the CPB sample, free water will no longer be discharged from the inside of the sample. Because the sample is not completely sealed, the increase of negative PWP is affected by the outside air, so the negative PWP gradually becomes stable (stage 3 shown in Fig. 15). Comparing the two PWP curves, the sample with drained curing condition has a larger negative PWP than that with undrained condition for more than half of the 1 day curing time. This difference in negative PWP causes the difference in the strength of the CPB.

The difference in strength caused by drainage conditions will inevitably lead to a difference in the shear parameters (internal friction angle, φ_b and cohesion, c_b) of the CPB. According to the calculation method of shear parameters mentioned above (formulas 1 to 4), Table 3 shows the calculated values of the shear parameters of the CPB samples when the curing time is 1 day under different drainage conditions. Compared to the undrained curing condition, the cohesion (c_b) of CPB under drained curing condition is increased from 71.80 kPa to 108.60 kPa (increased by 33.06%), while the corresponding internal friction angle (φ_b) is decreased from 44.72° to 42.78° (decreased by 4.12%).

Table 3 The calculated internal friction angle (φ_b) and cohesion (c_b) of CPB samples with curing time of 1 day under different drainage conditions.

Drainage condition	Stress state (kPa)					Internal friction angle (φ_b/°)	Cohesion (c_b/kPa)
	S_{d0}	S_d	σ_c	$(\sigma_1+\sigma_c)/2$	$(\sigma_1-\sigma_c)/2$	$\sin^{-1}B$	$A/(\cos\varphi_b)$
Drained	348.34	348.34	0	174.17	174.17	44.72	71.80
		512.67	35	293.34	256.34		
		677.71	70	408.86	338.86		
		844.14	105	527.07	422.07		
Undrained	508.58	480.34	0	240.17	240.17	42.78	108.60
		705.11	48	400.56	352.56		
		965.30	96	578.65	482.65		
		1056.11	144	672.06	528.06		

3.3. Influence of curing temperature on the triaxial compressive behaviors

In practice the curing temperatures of the CPB structure vary. There are many reasons causing difference in curing temperature, such as: (a) the geographic location of the mine; (b) seasonal changes in climate; (c) the depth of the mine-out area (the influence caused by the geothermal gradient); (d) the temperature rise caused by the heat of hydration of the CPB structure,

etc. Therefore, the CPB slurry backfilled to the mine-out area is often cured under different temperatures in different mines, which warrants the necessity of investigating the influence of curing temperatures on the triaxial compressive behaviors of CPB design.

Figs. 16 shows the typical deviator stress *versus* axial strain curves of CPB samples at curing temperatures of 35°C and 45°C for 1-day curing time (also refer Fig. 3(a) with 20°C curing temperature). The relevant curves with a specific lateral constraint ratio (σ_c/S_{d0}) are similar to one another at different curing temperatures. The lateral constraint ratio (σ_c/S_{d0}) determines the shape of the tested curves. The peak deviator stress and the ultimate axial strain (the axial strain required to reach to the peak deviator stress) always increase with the increase of σ_c/S_{d0}, irrelevant to the curing temperature changes.

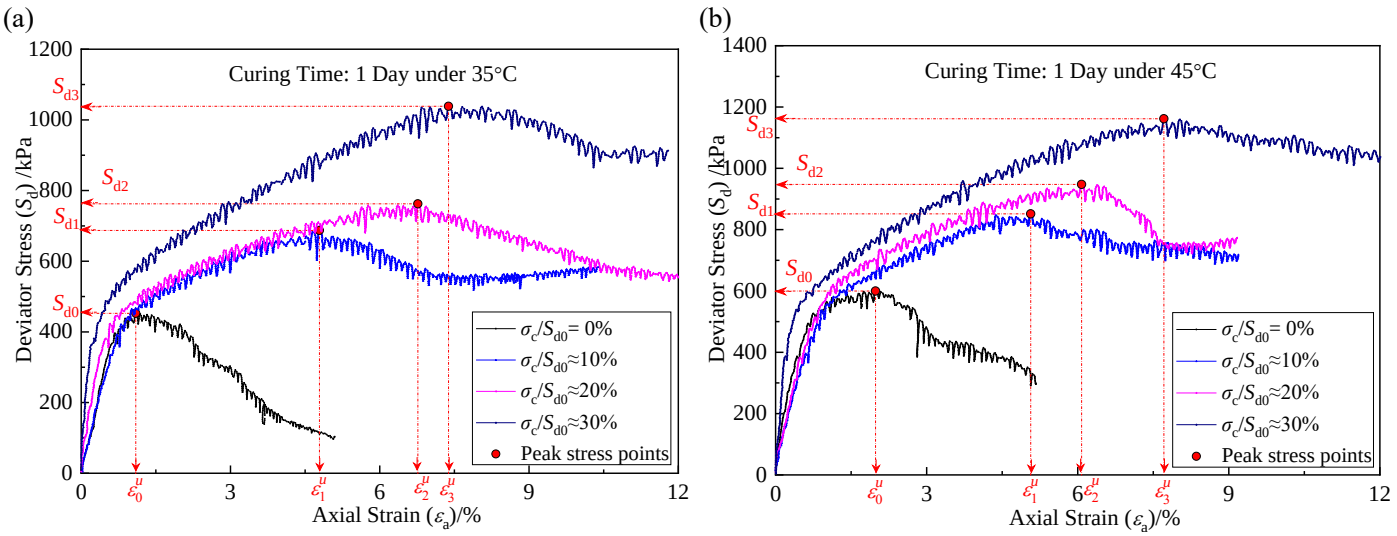

Fig.16 The typical deviator stress *versus* axial strain curves of CPB samples with 1-day curing time at different curing temperature: (a) at 35°C; (b) at 45°C.

The peak deviator stress is a key indicator to measure the strength of CPB structure, and curing temperatures have significant influences on the peak deviator stress. Fig. 17 shows the relationship between the different σ_c/S_{d0} values and the peak deviator stresses under different curing temperatures. It was observed previously that the peak deviator stress increases linearly with the increase of σ_c/S_{d0} at curing temperature of 20°C (Fig. 5(a) & Fig. 13 (a)). This linear relationship is also true for curing temperatures of 35°C and 45°C, as shown in Fig. 17(a). And the higher the curing temperature, the greater the value of peak deviator stress. This is because that the higher curing temperature can accelerate the hydration reaction of the binder in the CPB slurry. At a higher curing temperature, more hydration products (for example: hydrated calcium silicate gel (C-H-S), calcium hydroxide (C-H)) will be generated to bind the solid particles tightly, leading to higher strength (Xu et al., 2021; Sada and Fall, 2020; Fang and Fall, 2020). Moreover, more hydrated products will fill the voids between solid particles, making the CPB structure more compact, which is one of the reasons for increasing the CPB strength (Fang and Fall, 2018; Fall and Pokharel, 2010).

The ultimate axial strain can reflect the ductility (ability to resist deformation) of the CPB sample. Fig. 18 shows the

relationship between the σ_c/S_{d0} and the ultimate axial strain at different curing temperatures. The curing temperatures have a relatively small influence on the peak ultimate axial strain. However, the lateral constraint ratio σ_c/S_{d0} is clearly more sensitive to the ultimate axial strain. Similar to the different curing time (Fig. 6) and drainage conditions (Fig. 13b), the ultimate axial strain shows a negative exponential relationship with the increase of the σ_c/S_{d0}. In other words, the existence of the lateral constraint can significantly affect the deformability of the CPB sample.

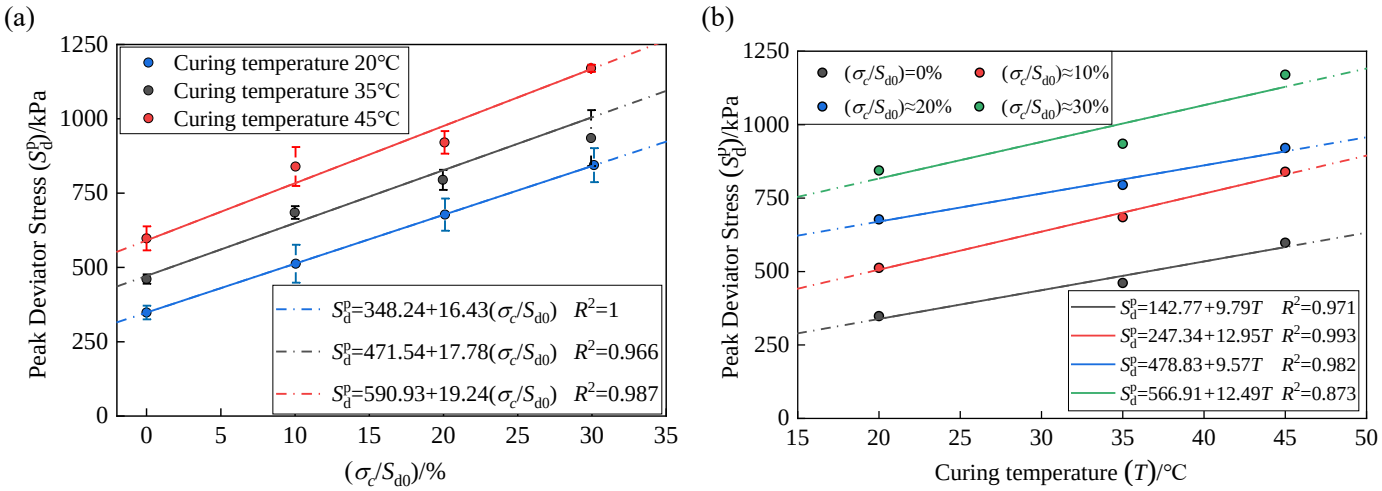

Fig.17 The relationship between different σ_c/S_{d0} values and peak deviator stresses under different curing temperatures (a) the relationship between σ_c/S_{d0} and peak deviator stress; (b) the relationship between curing temperature and peak deviator stress.

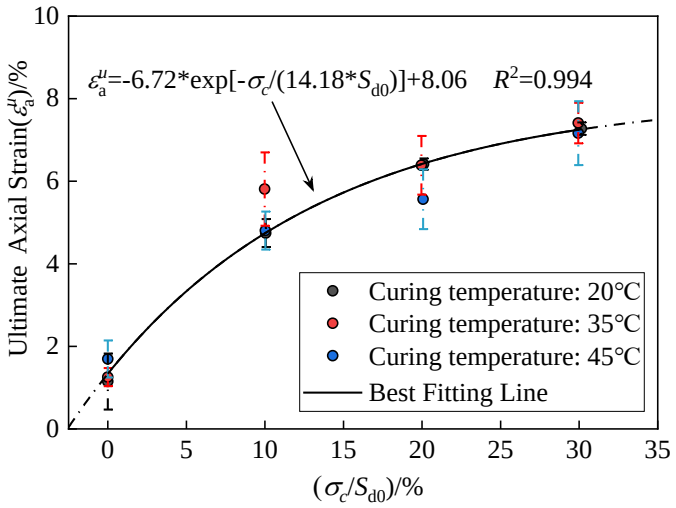

Fig.18 The relationship between the σ_c/S_{d0} and the ultimate axial strain at different curing temperatures.

The internal friction angle (φ_b) and cohesion (c_b) are also important shear mechanical parameters for CPB structures. These parameters are widely used in the calculation of various arching theoretical models and numerical analysis. Based on the calculation method of shear parameters given above (formulas 1~4), Table 4 gives the calculation results of the internal friction angle (φ_b) and cohesion (c_b) for CPB samples at different curing temperatures. From the calculated results in Table 4, the parameter S_{d0} (represent the unconfined compressive strength, UCS) is increased with the increase of curing temperature. Moreover, the internal friction angle (φ_b) and cohesion (c_b) of the tested CPB samples showed a linear decrease and increase with the curing temperature, respectively (as shown in Fig. 19).

Table 4 The calculated internal friction angle (φ_b) and cohesion (c_b) under different curing temperature.

Cruing temperature (°C)	Stress state (kPa)					Internal friction angle (φ_b/°)	Cohesion (c_b/kPa)
	S_{d0}	S_d	σ_c	$(\sigma_1+\sigma_c)/2$	$(\sigma_1-\sigma_c)/2$	$\sin^{-1}B$	$A/(\cos\varphi_b)$
20	348.34	348.34	0	174.17	174.17	44.72	71.80
		512.67	35	293.34	256.34		
		677.71	70	408.86	338.86		
		844.14	105	527.07	422.07		
35	460.95	460.95	0	230.47	230.47	38.92	116.00
		684.80	46	388.40	342.40		
		794.68	92	489.34	397.34		
		935.20	138	605.60	467.60		
45	597.96	597.96	0	298.98	298.98	37.27	150.20
		839.55	60	479.78	419.78		
		920.62	120	580.31	460.31		
		1170.05	179	764.03	585.03		

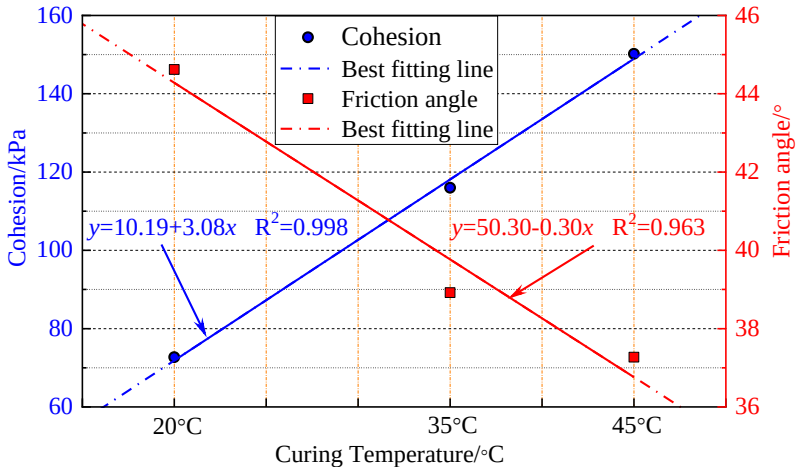

Fig.19 The relationship between the calculated shear parameters (internal friction angle, φ_b and cohesion, c_b) and the different curing temperatures.

Same as the factor of curing time, the regression model also can be established to predict the peak deviator stress. It can be seen from Fig. 17a that there is a clear linear relationship between the peak deviator stress and the σ_c/S_{d0} (therefore, it can be expressed by y=ax+b, y is the peak deviator stress; x is the σ_c/S_{d0}). And the parameters a and b are related to the curing temperature in this section. Therefore, it is necessary to establish the relationship between the fitting parameters a, b and the curing temperature to obtain the peak deviator stress regression model (shown in Fig.20). In the established regression model, the curing temperature (T) will be set as a variable. S_{d0} has an obvious linear relationship with the increase of the curing temperature (the black line in Fig. 17b). Then, putting the fitting relationship of the above parameters (a, b and S_{d0}) into the linear formula (y=ax+b), the peak deviator stress calculation model will be obtained as following:

$$\begin{aligned} S_d^p &= a + b\cdot(\sigma_c / S_{d0})\cdot 100\% \\ &= \frac{\sigma_c}{\xi_{1t}+\xi_{2t}T}(\xi_{3t}T+\xi_{4t})\cdot 100\% + \xi_{5t}T + \xi_{6t} \end{aligned} \tag{6}$$

Also, ξ_{1t}~ξ_{6t} are the corresponding fitting parameters in the formula 6. Formula 6 can realize the prediction of the peak deviator stress of CPB at given depth (it can be equivalent to the parameter σ_c) under different curing temperatures.

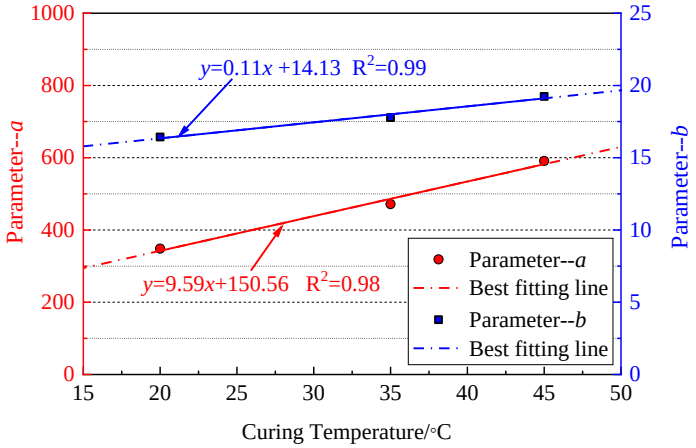

Fig.20 The fitting relationship between parameters (a, b) and curing temperature.

Fig. 21a shows the comparison of peak deviator stress between the calculated values obtained by formula 6 and the measured values. It can be seen from Fig. 21a that the measured peak deviator stress values are scattered on both sides of the straight line but very close to the line where the measured values equal to the calculated values. This shows that the calculation model can predict the peak deviator stress of the CPB structure well under different curing temperatures (T). In addition, formula 6 can be also used to predict the peak deviator stress values at different depths (σ_c). Therefore, the predicted internal friction angle (φ_b) and cohesion (c_b) values can be obtained. Fig. 21b indicates that the calculation model can effectively predict the internal friction angle (φ_b) and cohesion (c_b) of CPB, which are important parameters for the stability of CPB structures.

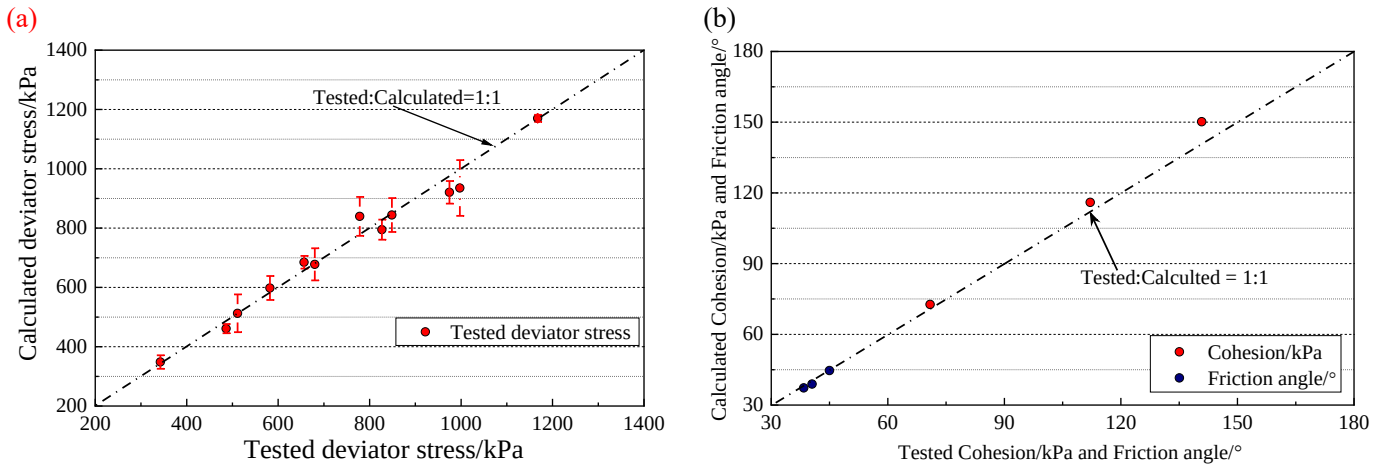

Fig.21 Comparative analysis of calculated and tested results: (a) the peak deviator stress; (b) the shear parameters (internal friction angle, φ_b and cohesion, c_b).

3.4. Typical failure pattern of CPB under different curing time, drainage conditions and curing temperatures

The peak deviator stress and the ultimate axial strain are directly linked to the failure pattern of CPB samples. Table 5 shows the typical failure patterns of CPB samples with various forms of cracks after triaxial compressive test under different curing time, drainage conditions and curing temperatures. These cracks can be roughly divided into three types: vertical tensile cracks (TC), shear cracks (SC) and derived micro cracks (MC). The three typical cracks was shown in table 5 (20℃, 1 day, undrained curing condition) as an example.

Table 5 The typical failure patterns of CPB samples under different curing time, drainage conditions and curing temperatures.

Category	Curing condition	σ_c/S_{d0}				Tested internal friction angle	Calculated shear failure angle
		=0%	≈10%	≈20%	≈30%	φ_b/°	θ_c/°
A	20°C, 1 day, undrained	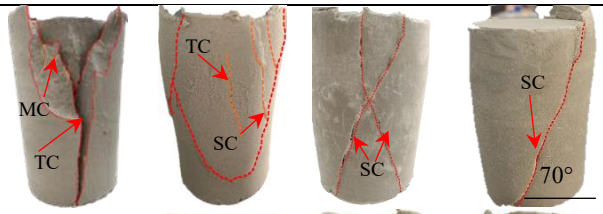				44.72	67.35
	20°C, 3 days, undrained					41.67	65.84
	20°C, 7 days, undrained					40.70	65.35
	20°C, 28` undrained	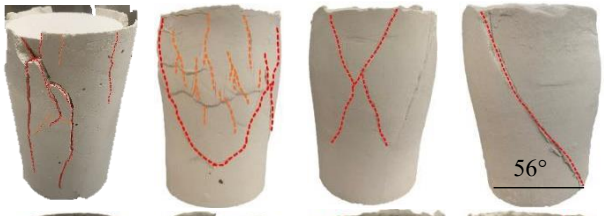				38.26	64.13
B	20°C, 1 day, drained					42.78	66.39
C	35°C, 1 day, undrained	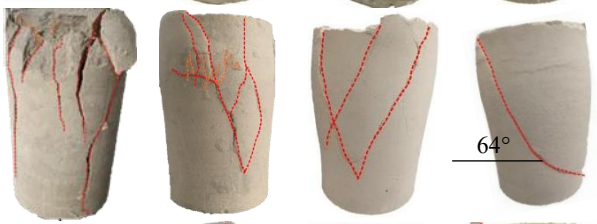				38.92	64.46
	45°C, 1 day, undrained					37.27	63.64

In general, different curing conditions have little effects on the failure pattern of CPB (shown in Table 5) under the same σ_c/S_{d0}. But σ_c/S_{d0} plays a key role on the failure pattern. The failure of CPB sample is dominated by tensile failure when the σ_c/S_{d0}=0%. Dense and large vertical tensile cracks are distributed on the surface for the damaged samples. Moreover, a small number of micro cracks were produced without lateral constraint stress (i.e., σ_c/S_{d0}=0%). When the $\sigma_c/S_{d0}\neq$0%, with the

increase of σ_c/S_{d0}, the number of cracks decreases, and the vertical tensile cracks and micro cracks gradually disappear, and then the obvious shear failures appear. Moreover, the dense cracks are widely distributed on the top of the tested CPB samples, the reason for this phenomenon is the uniform deformation of the CPB sample during the loading process (Xiu et al., 2020). When the $\sigma_c/S_{d0} \neq 0\%$, the lateral constraint stress can limit the lateral deformation of the CPB sample during the loading process. Therefore, the development of tensile cracks can also be limited by the lateral constraint stress. And the shear creaks will be gradually produced. Both the tensile cracks and shear cracks can be seen in the failure surface, when the $\sigma_c/S_{d0} \approx 10\%$. However, as the increase of the σ_c/S_{d0}, the tensile cracks disappear and only shear cracks were observed on the surfaces (i.e. $\sigma_c/S_{d0} \approx 20\%$ and 30%). When t$\sigma_c/S_{d0} \approx 30\%$, all the failure pattern of CPB samples show a single shear creak. The shear failure angle (single shear cracks, refer to $\sigma_c/S_{d0} \approx 30\%$ in Table 5) can be calculated by $\theta_c = 45° + \varphi_b/2$ (Fu et al., 2016). The calculated shear failure angle (θ_c) shown in Table 5 is close to the tested failure angle. In summary, as σ_c/S_{d0} the increase (from 0% to 30%), the failure patterns are: tensile failure ($\sigma_c/S_{d0}=0\%$), tensile-shear mixed failure ($\sigma_c/S_{d0} \approx 10\%$) and shear failure ($\sigma_c/S_{d0} \approx 20\%$ and 30%).

4. Discussion

Laboratory experimental studies are often used to examine engineering applications and provide design guidance in practice. CPB structure is often used to resist the deformation of surrounding rock by its hardening strength. The mechanical behaviors of CPB can obviously affect the vertical stress distribution (σ_v) inside the CPB structure. Many typical arching theories are closely related to the shear mechanical parameters (internal friction angle, φ_b and cohesion, c_b) of CPB (Ting et al., 2011). In this section, based on the experimental results and the widely used arching theory, the arching effect calculation with different curing time, drainage conditions and curing temperatures will be discussed, respectively.

4.1. Typical arching theories of CPB structure

Presently Marston's cohesionless model (Marston, 1930) and the Terzaghi's cohesive model (Terzaghi, 1943) are widely adopted to calculate the arching effect of CPB structures. Marston's cohesionless model does not consider the influence of the cohesion of the surrounding rock-CPB interface, the calculated vertical stress distribution (σ_v) gradually decreases with the increase of the internal friction angle (φ_b). From the tested results in this study, the internal friction angle (φ_b) of the CPB samples decreases with the increase of curing time (Figs. 9 and 19). So, in theory when using the Marston's cohesionless model, as the curing time increases (φ_b decreases), the vertical stress distribution (σ_v) of the CPB structure will increase. However, numerous field studies show that the vertical stress distribution (σ_v) inside the CPB structure decreases with the curing time (Helinski et al., 2010; Thompson et al., 2012; Grabinsky et al., 2014). Therefore, Marston's cohesionless model has obvious limitations when the curing time is considered as a factor.

To include the cohesion in the arching theory, Terzaghi's cohesive model (modified from Marston's cohesionless model) was

proposed (Terzaghi, 1943). The basic assumptions for Terzaghi's cohesive model include: (1) the horizontal stress distribution at the given depth is uniform; (2) the internal friction angle and cohesion of the surrounding rock-CPB interface are equivalent to the corresponding internal friction angle and cohesion of the CPB (φ_b, c_b); and (3) the pore water pressure is not considered. Terzaghi's cohesive model can be expressed as (Cui and Fall, 2018):

$$\begin{aligned} \sigma_h &= \frac{\gamma_b B - 2c_b}{2\tan\varphi_b}[1-\exp(-\frac{2K_0\tan\varphi_b H}{B})] \\ \sigma_v &= \sigma_h / K_0 \\ K_0 &= 1-\sin\varphi_b \end{aligned} \tag{7}$$

Where, σ_h is the horizontal stress; γ_b is the unit weight of CPB; B and H are the width and height of the mined-out area; σ_v is the vertical stress; φ_b and c_b are the internal friction angle and cohesion of CPB; K_0 is the earth-pressure coefficient.

4.2. Application of Terzaghi's cohesive model for CPB structures under different curing conditions

With Terzaghi's cohesive model (formula 7), the corresponding model parameters can be summarized into two categories: (a) geometric parameters of mined-out area and (b) the mechanical parameters of CPB. For a given mined-out area, the geometric parameters are fixed. Therefore, it is necessary to focus on the mechanical parameters of CPB. This section will use the mechanical parameters (refer to internal friction angle, φ_b and cohesion, c_b)) of CPB structures obtained by experimental study to discuss the vertical stress distribution (σ_v, calculated by Terzaghi's cohesive model) inside the CPB structure.

Using the geometric parameters of the mined-out area (H=100 m, B=20 m) mentioned in Wei et al., (2020), Fig. 22 shows the distribution of the vertical stress along the depth under different curing conditions. It can be seen from Fig. 22 that regardless of the curing conditions of CPB, the vertical stress distribution calculated by the Terzaghi's cohesive model is much smaller than the CPB's overburden pressure (calculated by $\gamma_b \cdot H$). The vertical stress distribution gradually decreases with the increase of curing time (as shown in Fig. 22a), which means that the arching effect inside the CPB structure gradually increases. This reassures that Terzaghi's cohesive model can predict time-enhancing effect. It should be clearly pointed out that when the curing time is 28 days, the tested cohesion (c_b) of the CPB is 234.90 kPa (shown in table 2), and the calculated $\gamma_b B - 2c_b < 0$. The vertical stress distribution calculated by the Terzaghi's model is $\sigma_v < 0$, which is not in line with the actual situation. To mitigate this issue, Ting et al. (2011) proposed a formula to limit the cohesion (c_b) range of CPB, as formula (8).

$$0 \le c_b \le \frac{\gamma_b B}{2} \tag{8}$$

Also, due to the difference in drainage conditions and temperature during the curing process of a CPB slurry backfilled into the mined-out area, the mechanical parameters of the CPB will be different. This in turn will affect the vertical stress distribution of the CPB structure. It can be seen from Fig. 22b that the vertical stress distribution inside the CPB structure under the drained curing condition is significantly smaller than that under the undrained condition. This is the fact that the dissipation rate of PWP inside the CPB slurry is accelerated (as shown in the Fig. 15). And the mechanical properties (e.g., peak deviator stress and cohesion, c_b) of CPB are also improved under the drained curing condition (shown in Fig. 13 and

table 3). With the increase of the curing temperatures, the vertical stress distribution inside the CPB structure gradually decreases (shown in Fig. 22c). Such calculated results do indicate that the significant temperature-enhancing effect exists.

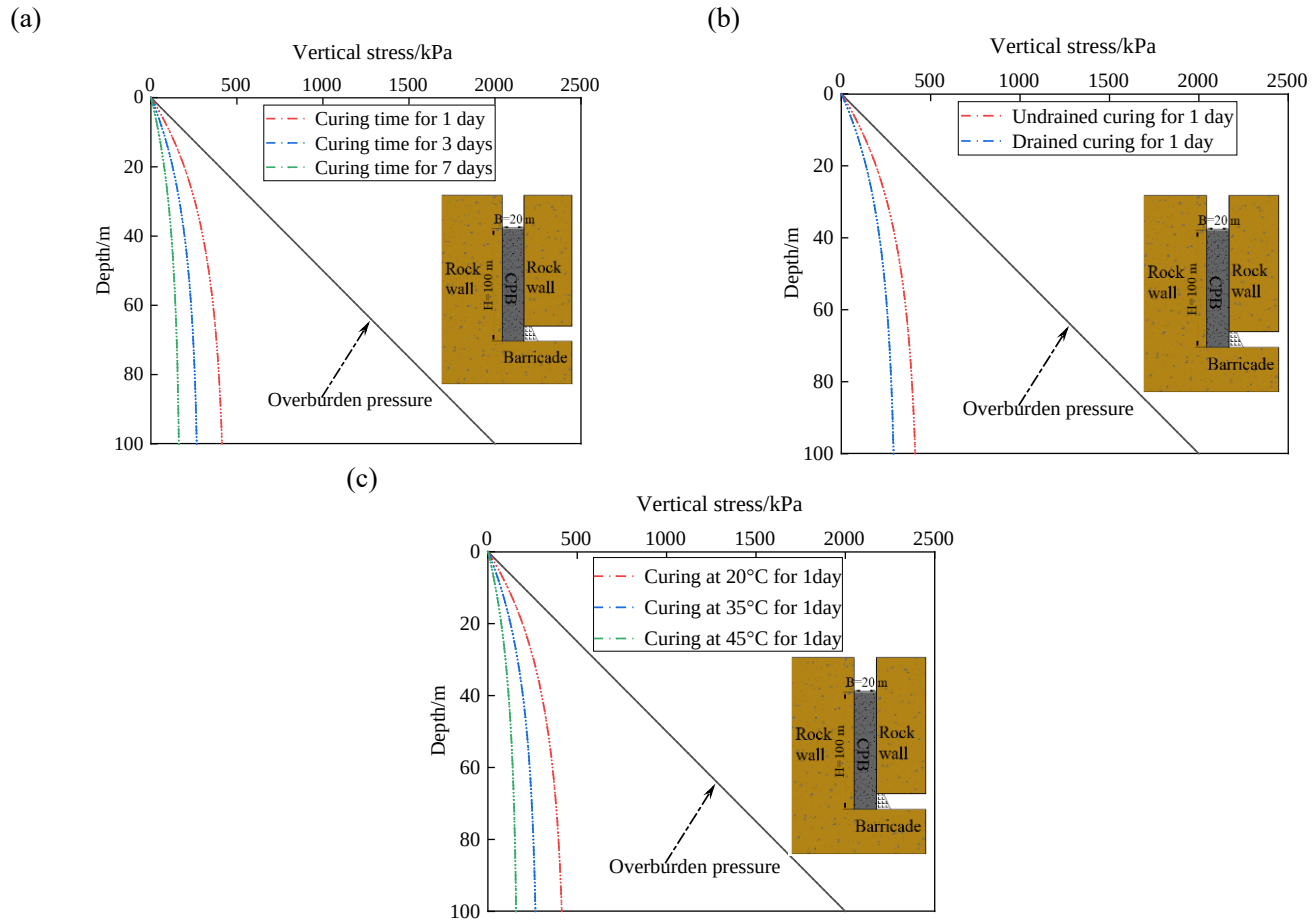

Fig.22 Comparison of vertical stress for different curing conditions (note that: H=100 m, B=20 m, γ_b=20 kN/m^3; the value of parameter γ_b is an approximation referenced from Ting et al., 2010): (a) different curing time (1, 3 and 7 days); (b) different drainage conditions (drained and undrained); (c) different curing temperatures (20 ℃, 35℃ and 45 ℃).

5. Summary and conclusions

To better understand the triaxial mechanical properties of CPB, this work carried out the triaxial compression tests to investigate the effects of different curing times (1, 3, 7 and 28 days), drainage and undrained curing conditions, different curing temperatures (20 ℃, 35℃ and 45 ℃) on triaxial mechanical properties of CPB. The following conclusions are drawn:

- The changing trends of measured deviator stress *versus* axial strain curves for CPB samples are determined by the lateral constraint ratio (σ_c/S_{d0}). And as the σ_c/S_{d0} increases, the obvious elastoplastic stage (or elastoplastic deformation) was observed. The different curing conditions have less effect on the tested curves and ultimate axial strain. Regardless of the curing conditions, the peak deviator stress presents an obvious linear increase with the increase of σ_c/S_{d0} , in the meanwhile the ultimate axial strain increases exponentially.
- With the increase of curing time, the internal friction angle (φ_b) showed an exponential decrease, and the cohesion (c_b) showed an increase. The established regression formula can well predict the triaxial mechanical parameters (i.e., peak

deviator stress, cohesion, and internal friction angle) of CPB under different curing time.

- CPB samples cured under drained condition can hold on a relatively larger negative pore water pressure (PWP) than that of undrained condition. Also, duo to the larger negative PWP under drained condition, the higher compressive strength of CPB sample was generated. Compared with the drained curing condition, the undrained curing condition caused the internal friction angle (φ_b) and cohesion (c_b) of CPB sample to decrease 1.84% and increase 33.06% respectively.
- Increasing curing temperature can lead to higher compressive strength (a linear relationship). With the increase of curing temperature, the internal friction angle (φ_b) decreases but the cohesion (c_b) increases. The established regression formula with curing temperature as a variable can effectively predict the corresponding mechanical parameters of CPB.
- As the increase of σ_c/S_{d0}, the failure modes of CPB sample can be divided into tensile failure (σ_c/S_{d0}=0%) → mixed tensile-shear failure (σ_c/S_{d0}≈10%) → compression-shear failure (σ_c/S_{d0}≥20%). The cracks on the surface gradually decrease with the increase of σ_c/S_{d0}, and then, the tensile cracks gradually disappear. Eventually, only the shear cracks are shown on the sample surfaces.

The different mechanical parameters of CPB play a key role in the stress distribution inside the backfilled CPB structure. Therefore, a better understanding of the triaxial mechanical properties of CPB under different curing times and conditions has guiding significance for the backfilled engineering in practice. It is hoped that the findings of this study can provide data and theoretical supports for CPB design and applications.

CRediT authorship contribution statement

Zhanguo Xiu: Data curation, Results and discussion, Writing - original draft. **Shuhong Wang:** Conceptualization, Methodology, Funding acquisition, Resources. **Yingchun Ji:** Final editing, Writing - review & editing. **Feili Wang:** Data analysis, Results and discussion, Writing - original draft. **Fengyu Ren:** Project administration, Writing - review & editing. **Van-Tuan Nguyen:** Writing - review & editing.

Declaration of Competing Interest

The authors declare that they have no known competing financial interests or personal relationships that could have appeared to influence the work reported in this paper.

Acknowledgments

This work was conducted with supports from the National Natural Science Foundation of China (Grant Nos. U1602232 and (51474050), Liaoning Science and Technology Project (2019JH2/10100035). Also, the authors would like to thank PhD. Haiqiang Jiang for supplying the silica tailings and tested molds.

References

ASTM C143/C143M-15, 2015. Standard Test Method for Slump of Hydraulic-Cement Concrete. ASTM International, West

Conshohocken, PA.

ASTM D2487-17e1, 2017. Standard Practice for Classification of Soils for Engineering Purposes (Unified Soil Classification System). ASTM International, West Conshohocken, PA.

Behera, S.K., Ghosh, C.N., Mishra, D.P., Singh, P., Mishra, K., Buragohain, J., Mandala, P.K., 2020. Strength development and microstructural investigation of lead-zinc mill tailings based paste backfill with fly ash as alternative binder. Cem. Concr. Compos. 109, 103553.

Belem, T., Benzaazoua, M., Bussière, B., 2000. Mechanical behaviour of cemented paste backfill. Proceedings of the 53rd Canadian Geotechnical Conference, Montreal, Que., Canada. Oct. 15-18, 373-380.

Bull, A.J., Fall, M., 2020. Curing temperature dependency of the release of arsenic from cemented paste backfill made with Portland cement. J. Environ. Manage. 269, 110772.

Cao, S., Song, W., 2017. Effect of filling interval time on the mechanical strength and ultrasonic properties of cemented coarse tailing backfill. Int. J. Miner. Process. 166, 62-68.

Cao,S., Yilmaz, E., Yin, Z., Xue, G., Song, W., Sun, L., 2021. CT scanning of internal crack mechanism and strength behavior of cement-fiber-tailings matrix composites. Cem. Concr. Compos. 116, 103865.

Chen, Q., Zhang, Q., Qi, C., Fourie, A., Xiao, C., 2018. Recycling phosphogypsum and construction demolition waste for cemented paste backfill and its environmental impact. J. Clean. Prod. 186, 418-429.

Cui, L., Fall, M., 2018. Mathematical modelling of cemented tailings backfill: a review. Int. J. Min. Reclam. Env. 42 (3), 558-583.

Deng, D., Liu, L., Yao, Z., Song, K.I., Lao, D., 2017. A practice of ultra-fine tailings disposal as filling material in a gold mine. J. Environ. Manage. 196, 100-109.

Ercikdi, B., Kesimal, A., Cihangir, F., Deveci, H., Alp, İ., 2009. Cemented paste backfill of sulphide-rich tailings: Importance of binder type and dosage. Cem. Concr. Compos. 31 (4), 268-274.

Ercikdi, B., Yilmaz, T., Külekçi, G., 2016. Strength and ultrasonic properties of cemented paste backfill. Ultrasonics. 54, 195-204.

Fall, M., Belem, T., Samb, S., Benzaazoua, M., 2007. Experimental characterization of the stress–strain behaviour of cemented paste backfill in compression. J. Mater. Sci. 42(11), 3914-3922.

Fall, M., Nasir, O., 2010. Mechanical behaviour of the interface between cemented tailings backfill and retaining structures under shear loads. Geotech. Geol. Eng. 28(6), 779-790.

Fall, M., Pokharel, M., 2010. Coupled effects of sulphate and temperature on the strength development of cemented tailings backfills: Portland cement-paste backfill. Cem. Concr. Comp. 32 (10), 819-828.

Fang, K., Cui, L., 2020. M. Fall, A coupled chemo-elastic cohesive zone model for backfill-rock interface. Comput. Geotech.

125, 103666.

Fang, K., Fall, M., 2018. Effects of curing temperature on shear behaviour of cemented paste backfill-rock interface. Int. J. Rock Mech. Min. Sci. 112, 184-192.

Fang, K., Fall, M., 2019. Chemically induced changes in the shear behaviour of interface between rock and tailings backfill undergoing cementation. Rock Mech. Rock Eng. 52 (9), 3047-3062.

Fang, K., Fall, M., 2020. Shear Behavior of the Interface Between Rock and Cemented Backfill: Effect of Curing Stress, Drainage Condition and Backfilling Rate. Rock Mech. Rock Eng. 53, 325-336.

Fang, K., Fall, M., 2020. Insight into the mode I and mode II fracture toughness of the cemented backfill-rock interface: Effect of time, temperature and sulphate. Constr. Build. Mater. 262, 120860.

Fu, J., Song, W., Tan, Y., 2016. Study on microstructural evolution and strength growth and fracture mechanism of cemented paste backfill. Adv. Mater. Sci. Eng. 2016, 8792817.

Ghirian, A., Fall, M., 2013. Experimental investigation on thermo-hydro-mechanical-chemical behaviour of cemented paste backfill, 23rd world mining congress and expo. Montreal, Canada, Aug. 11-15, 378.

Grabinsky, M.W., Simon, D., Thompson, B.D., Bawden, W.F., Veenstra, R.L., 2014. Interpretation of as-placed cemented paste backfill properties from three mines. 11th International Symposium on Mining with Backfill. Australian Centre for Geomech., Perth, Australia.

Helinski, M., Fahey, M., Fourie, A., 2010. Behavior of Cemented Paste Backfill in Two Mine Stopes: Measurements and Modeling. J. Geotech. Geoenviron. Eng. 137 (2), 171-182.

Hou, C., Zhu, W., Yan, B., Guan, K., Du, J., 2018. Influence of binder content on temperature and internal strain evolution of early age cemented tailings backfill. Constr. Build. Mater. 189(20), 585-593.

Hou, C., Zhu, W., Yan, B., Guan, K., Du, J., 2020. The effects of temperature and binder content on the behavior of frozen cemented tailings backfill at early ages. Constr. Build. Mater. 239, 117752.

Jiang, H., Fall, M., Cui, L., 2016. Yield stress of cemented paste backfill in sub-zero environments: experimental results. Miner. Eng. 92, 141-150.

Jiang, H., Qi, Z., Yilmaz, E., Han, J., Qiu, J., Dong, C., 2019. Effectiveness of alkaliactivated slag as alternative binder on workability and early age compressive strength of cemented paste backfills. Constr. Build. Mater. 218, 689-700.

Jiang, H., Yi, H., Yilmaz, E., Liu, S., Qiu, J., 2020. Ultrasonic evaluation of strength properties of cemented paste backfill: Effects of mineral admixture and curing temperature. Ultrasonics. 100, 105983.

Li, W., Fall, M., 2016. Sulphate effect on the early age strength and self-desiccation of cemented paste backfill. Constr. Build. Mater. 106, 296-304.

Liu, Q., Liu, D., Tian, Y., Liu, X., 2017. Numerical simulation of stress-strain behaviour of cemented paste backfill in triaxial

compression. Eng. Geol. 231, 165-175.

Ma, D., Duan, H., Liu, J., Li, X., Zhou, Z., 2019. The role of gangue on the mitigation of mining-induced hazards and environmental pollution: An experimental investigation. Sci. Total Environ. 664, 636-1448.

Marston, A., 1930. The theory of external loads on closed conduits in the light of the latest experiments. Proceedings of the 9th Annual Meeting of the Highway Research Board, Vol. 9, Highway Research Board.

Nasir, O., Fall, M., 2008. Shear of cemented pastefill-rock interfaces. Eng. Geol. 101 (3), 146-153.

Orejarena, L., Fall, M., 2010. The use of artificial neural networks to predict the effect of sulphate attack on the strength of cemented paste backfill. Bull. Eng. Geol. Environ. 69 (4), 659-670.

Pokharel, M., Fall, M., 2010. Coupled thermo-chemical effects on the strength development on Slag-Paste backfill materials. ASCE J. Mater. Civil Eng. 23 (5), 511-525.

Qi, C., Fourie, A., 2019. Cemented paste backfill for mineral tailings management: Review and future perspectives. Miner. Eng. 144, 106025.

Rankine, R.M., Sivakugan, N., 2007. Geotechnical properties of cemented paste backfill from Cannington Mine, Australia. Geotech. Geol. Eng. 25, 383-93.

Sada, H., Fall, M., 2020. Time- and temperature-dependent rheological properties of cemented paste backfill that contains superplasticizer. Powder Technol. 360, 731-740.

Simms, P., Grabinsky, M., 2009. Direct measurement of matric suction in triaxial tests on early-age cemented paste backfill. Can. Geotech. J. 46, 93-101.

Simon, D., Grabinsky, M., 2013. Apparent yield stress measurement in cemented paste backfill, Int. J. Min. Reclam. Env. 27(4), 231-256.

Terzaghi, K., 1943. Theoretical Soil Mechanics. Wiley and Sons, Hoboken, NJ.

Thompson, B.D., Bawden, W.F., Grabinsky, M.W., 2012. In-situ Measurements of Cemented Paste Backfill at the Cayeli Mine, Can. Geotech. J. 49 (7), 755-772

Ting, C., Shukla, S.K., Sivakugan, N., 2011. Arching in soils applied to inclined mine stopes. Int. J. Geomech. 11 (1), 29-35.

Wang, J., Fu, J., Song, W., 2020. Mechanical properties and microstructure of layered cemented paste backfill under triaxial cyclic loading and unloading. Constr. Build. Mater. 257, 119540.

Wei, X., Guo, L., Zhou, X., Li, C., Zhang, L., 2020. Study on the stress evolution law and prediction model of high stage cemented backfill during full sequence period. Rock Soil Mech. 41 (11), 3613-3620.

Wu, J., Feng, M., Chen, Z., Mao, X., Han, G., Wang, Y., 2018. Particle Size Distribution Effects on the Strength Characteristic of Cemented Paste Backfill. Minerals. 8(8), 322.

Wu, J., Jing, H., Yin, Q., Meng, B., Han, G., 2020a. Strength and ultrasonic properties of cemented waste rock backfill

considering confining pressure, dosage and particle size effects. Constr. Build. Mater. 242, 118132.

Wu, J., Jing, H., Yin, Q., Yu, L., Meng, B., Li, S., 2020b. Strength prediction model considering material, ultrasonic and stress of cemented waste rock backfill for recycling gangue. J. Clean. Prod. 276, 123189.

Xu, W., Liu, B., Wu, W., 2020. Strength and deformation behaviors of cemented tailings backfill under triaxial compression. J. Cent. South Univ. 27(12), 3531-3543

Xiu, Z., Wang, S., Ji, Y., Wang, F., Ren, F., 2020. Experimental investigation on liquefaction and post-liquefaction deformation of stratified saturated sand under cyclic loading. Bull. Eng. Geol. Environ. 79, 2313-2324.

Xiu, Z., Wang, S., Ji, Y., Wang, F., Ren, F., Nguyena, V., 2021. The effects of dry and wet rock surfaces on shear behavior of the interface between rock and cemented paste backfill. Powder Technol. 381, 324-337.

Xiu, Z., Wang, S., Ji, Y., Wang, F., Ren, F., Nguyena, V.T., 23020. Loading rate effect on the uniaxial compressive strength (UCS) behavior of cemented paste backfill (CPB). Constr. Build. Mater. 271, 121526.

Xu, W., Chen, W., Tian, M., Guo, L., 2021. Effect of temperature on time-dependent rheological and compressive strength of fresh cemented paste backfill containing flocculants. Constr. Build. Mater. 267, 121038.

Xu, W., Zhang, Y., Liu, B., 2020. Influence of silica fume and low curing temperature on mechanical property of cemented paste backfill. Constr. Build. Mater. 254, 119305.

Xu, W., Zhang, Y., Zuo, X., Hong, M., 2020. Time-dependent rheological and mechanical properties of silica fume modified cemented tailings backfill in low temperature environment. Cem. Concr. Compos. 114, 103804.

Yang, L., Xu, W., Yilmaz, E., Wang, Q., Qiu, J., 2020. A combined experimental and numerical study on the triaxial and dynamic compression behavior of cemented tailings backfill. Eng. Struct. 219, 110957.

Yilmaz, T., Ercikdi, B., Karaman, K., Külekçi, G., 2014. Assessment of strength properties of cemented paste backfill by ultrasonic pulse velocity test. Ultrasonics. 52, 1386-1394.

Zhang, W., Gu, X., Qiu, J., Liu, J., Zhao, Y., Li, X., 2020. Effects of iron ore tailings on the compressive strength and permeability of ultra-high performance concrete. Constr. Build. Mater. 260, 119917.

Zhao, K., Yu, X., Zhu, S., Yan, Y., Zhou, Y., He, Z., Song, Y., Huang, M., 2020. Acoustic emission fractal characteristics and mechanical damage mechanism of cemented paste backfill prepared with tantalum niobium mine tailings. Constr. Build. Mater. 258, 119720.

Zhou, Y., Yu, X., Guo, Z., Yan, Y., Zhao, K., Wang, J., Zhu, S., 2020. On acoustic emission characteristics, initiation crack intensity, and damage evolution of cement-paste backfill under uniaxial compression. Constr. Build. Mater. 269, 121261.